Flow around in-line sphere array at moderate Reynolds number

Daehyun Choi, and Hyungmin Park

Citation: Physics of Fluids **30**, 097104 (2018); doi: 10.1063/1.5049734
View online: https://doi.org/10.1063/1.5049734
View Table of Contents: http://aip.scitation.org/toc/phf/30/9
Published by the American Institute of Physics

Flow around in-line sphere array at moderate Reynolds number

Daehyun Choi and Hyungmin Park[a)]
Department of Mechanical and Aerospace Engineering, Seoul National University, Seoul 08826, South Korea

(Received 25 July 2018; accepted 5 September 2018; published online 27 September 2018)

In the present study, we perform a series of water-tunnel experiments to investigate the flow around an in-line sphere array at the Reynolds number of 1000, based on the free-stream velocity and sphere diameter, focusing on how the sphere wake changes by the additional spheres located behind while the spacing between them being varied. We try to capture the qualitative picture of the wake behind each sphere and to measure quantitative distribution of flow statistics using dye visualization and particle image velocimetry techniques. When the spacing is less than one sphere diameter, the gap flow is steady and axisymmetric, while the last wake is planar symmetric with a weaker turbulence level. When the spacing is twice larger than the sphere diameter, on the other hand, the flows in the gap and final wake tend to recover the axisymmetric feature, which is similar to that of a single sphere wake at the same Reynolds number. Between these two regimes, there is a transitional flow regime (the spacing is comparable to the sphere diameter) where the flow is still planar symmetric, but the turbulence level is enhanced. Depending on the flow topology, it is found that the characteristic frequencies (i.e., Strouhal number) in the shear layers and the gap are also affected. Finally, based on our analysis, we propose a flow regime map for each wake in the considered sphere arrays and also estimate the pressure distribution from the velocity measurements, by which the forces acting on each sphere can be assessed. *Published by AIP Publishing.* https://doi.org/10.1063/1.5049734

I. INTRODUCTION

The flow around a bluff body (a circular cylinder or sphere, for example) has been investigated for a long time as one of the canonical problems in fluid mechanics (Williamson, 1996) due to its academic and practical importance. Despite its simple geometry, its general picture includes complex flow phenomena such as the growth of the boundary layer, separation (reattachment under certain conditions), shear-layer evolution (trigger of an instability), and vortex shedding in the wake, which has been quite well understood through many experimental, numerical, and theoretical studies (Achenbach, 1974; Monkewitz and Nguyen, 1987; Park *et al.*, 2006; Yun *et al.*, 2006; and Pier, 2008). Furthermore, it is a common occurrence associated with a fluid flow over an obstacle or induced by the movement of a natural or artificial object, in which the abovementioned flow features are strongly connected to the fluid forces acting on the body. Thus, many studies have been performed to develop an effective method to control the flow around a bluff body (Choi *et al.*, 2008). While our understanding of the flow around a single bluff body is firmly established, the cases where more than two bluff bodies (e.g., spheres) are closely located have not been fully investigated. Furthermore, the importance of flows around multiple bodies is perceived from many practical or applied problems of a recent interest involving the multi-body fluid interactions where the distance between the bodies is so close that the flow around a body is strongly affected by the wake of surrounding bodies (Blackman and Perret, 2016; Hamilton *et al.*, 2016; Shi and Christopher, 2016; Testik and Ungarish, 2016; and Kumar *et al.*, 2018). Relevant examples can also be found in liquid-gas two-phase flows in which the interaction between adjacent liquid droplets is critical to control their shedding for the purpose of water management in fuel cells (Kimball *et al.*, 2008), suppression of icing on the solid surface (Cebeci and Kafyeke, 2003), and removal of solid particles (Soltani and Ahmadi, 1994) or oil droplets (Madani and Amirfazli, 2014). In studying these problems, one needs to understand the effect of the wake behind a leading droplet on the flow around a trailing one. Similar issues exist in the flows involving particle-to-particle interactions. When two spherical particles aligned in-line closely move together, the trailing particle is attracted to the wake behind a leading one and changes its position to the side of the leading one or overtakes it, depending on the Reynolds number and spacing between them (Happel and Pfeffer, 1960; Fortes *et al.*, 1987; and Hooshanginejad and Lee, 2017).

As a fundamental problem to understand the fluid flow interactions in a multi-body configuration, the flow around two adjacent spheres have been widely investigated, which are arranged in in-line, side-by-side (tandem), and staggered configurations with respect to the free-stream direction (Tsuji *et al.*, 1982; Kim *et al.*, 1993; Zhu *et al.*, 1994; Liang *et al.*, 1996; Chen and Lu, 1999; Folkersma *et al.*, 2000; Tsuji *et al.*, 2003; Schouveiler *et al.*, 2004; Yoon and Yang, 2007; 2009; Prahl *et al.*, 2009; and Jadoon *et al.*, 2010). Among the different configurations, we are interested in the in-line arrangement because the flow disturbances by leading particles should propagate along the mean flow direction, and thus it is highly probable that any particles in a multi-body fluid

[a)]Author to whom correspondence should be addressed: hminpark@snu.ac.kr. Also affiliated with Institute of Advanced Machines and Design, Seoul National University, Seoul 08826, South Korea.

system are readily affected by the wakes of upstream particles. Uhlmann and Doychev (2014) reported that the most probable location of the neighboring particle appears along the flow direction behind the reference particle (displaced from 0.8 to 3 particle diameters), by simulating the sedimentation of suspension spherical particles.

When two spheres (whose diameter is D) are positioned in the in-line arrangement, the spacing (L) between them and the Reynolds number ($Re_D = u_\infty D/\nu$; u_∞ is the free-stream velocity, and ν is the kinematic viscosity of the fluid) are important parameters to determine the flow structures around them. For Re_D = 50–130 at which the wake behind a single sphere is steady axisymmetric, for example, a stagnant flow develops at the gap for L/D = 0–2.0, as the separating shear layer from the leading sphere re-attaches to the trailing one (Zhu *et al.*, 1994; Liang *et al.*, 1996; and Chen and Lu, 1999). The drag on the trailing sphere is significantly reduced, while that on the leading one remains almost unaffected. As the L/D increases beyond 2.0, the re-attachment disappears and the trailing sphere faces high momentum flow entrained by the leading sphere wake. Thus the drag on the trailing sphere increases and quickly converges to that on a single sphere as L/D increases. For Re_D = 300, where the planar symmetric hairpin vortex is shed periodically in the wake behind a single sphere (Johnson and Patel, 1999 and Sakamoto and Haniu, 1990), three flow regimes are identified depending on L/D (Tsuji *et al.*, 1982; Yoon and Yang, 2009; Zou *et al.*, 2005; and Prahl *et al.*, 2009). When spheres are in a close proximity ($L/D < 0.7$), a steady axisymmetric wake is formed behind each sphere. With $L/D > 1.3$, each wake shows a similar structure to that of a single sphere, i.e., a planar symmetric vortex shedding. Between these two regimes, there is a transitional regime ($0.7 < L/D < 1.3$) at which the wake structures are steady planar symmetric. For higher Reynolds numbers of Re_D = 800–3000, where the corresponding wake of a single sphere has large- and small-scale eddies originated from the recirculation bubble and shear layer, respectively (Sakamoto and Haniu, 1990 and Tomboulides and Orszag, 2000), there are few studies on the flow around in-line spheres. Tsuji *et al.* (1982) measured the drag force for a range of Re_D = 200–800 and argued that, depending on L/D, the drag coefficients of two spheres are similar to each other regardless of the Reynolds number, by comparing the data obtained for Re_D = 10 000 by Lee (1979). However, detailed investigation supporting their arguments has not been done and still many are unknown for the flow around in-line spheres at this moderate Re_D-regime.

Furthermore, for the flow around the in-line sphere array consisting of more than three spheres, the relevant information lacks, as well (Liang *et al.*, 1996 and Maheshwari *et al.*, 2006). They considered a relatively low Reynolds number range of $Re_D \simeq$ 1–100 and reported a successive decrease in the drag force on the spheres along the streamwise direction, when L/D = 3.0; however, it is reversed at $L/D < 1.0$ (the drag on the second sphere is smaller than that on the third one). However, for a higher Reynolds number range of $Re_D > 300$, no study has been performed to the best knowledge of ours for the flow around a multiple-sphere array. It is clear that the wake structure behind each sphere is determined by the combination of the Reynolds number (Re_D) and spacing between spheres (L/D). However, the number of spheres has been restricted to two and relatively low Reynolds numbers ($Re_D \leq \boldsymbol{O}(10^2)$) have been considered in most previous studies. Considering practical problems where the multi-body fluid interaction is important, it is first necessary to investigate the effects of the number of spheres (more than three). Not to mention the fact that the particle (bubble, droplet) Reynolds number of a complex two-phase flow rises up to the moderate values of $\boldsymbol{O}(10^3)$ (Hoomans *et al.*, 1996; Zhu *et al.*, 2007; Jeong and Park, 2015; Kim *et al.*, 2016; and Lee and Park, 2017), it is meaningful to increase the Reynolds number of interest because the flow around a single sphere significantly changes when Re_D exceeds 800, in terms of the dynamics of hairpin vortices in the wake (Sakamoto and Haniu, 1990 and Tomboulides and Orszag, 2000).

Therefore, in the present study, we experimentally study the interaction between the wake flows of a fixed in-line sphere array while varying the number (1-5) of spheres and the spacing (L/D = 0–3.0), at the Reynolds number of Re_D = 1000 where the single sphere wake has an irregular vortex shedding due to the co-existence of large- and small-scale vortices (Kim and Durbin, 1988). The experiments are performed in a circulating water tunnel. To identify and characterize the flow structures, we use a dye visualization to capture the three-dimensional structure of the flow and perform particle image velocimetry measurement to obtain quantitative data such as the instantaneous flow field, time-averaged flow characteristics, Strouhal number, and pressure field estimated from the velocity distribution. Combining the qualitative and quantitative measurements on the flow, we will suggest a comprehensive flow regime map for the flow around the in-line sphere array in terms of the spacing and number of spheres. We believe that this will further our understanding on the multi-body fluid interaction that can be extended to various problems, e.g., multiphase flows.

The paper is organized as follows. In Sec. II, we explain the experimental setup including a water tunnel facility to precisely locate the multiple spheres at the required positions and flow measurement techniques. In Sec. III, we will first introduce the flow around a single sphere at the considered condition, which is followed by the cases of multiple spheres in Sec. IV. A detailed analysis on the instantaneous and time-averaged flow fields is presented. Combining the results, we estimate the pressure field based on the velocity measurements and suggest a flow regime map for the present configuration in Sec. V, and finally, our results and conclusions are summarized in Sec. VI.

II. EXPERIMENTAL SETUP AND PROCEDURE

A. Flow facility and sphere array

The experiments are conducted in a small-sized circulating-type water-tunnel, as shown in Fig. 1(a), of which the test section [600 mm × 80 mm × 80 mm in the streamwise (x), vertical (y), and transverse (z) directions, respectively] is made of 10 mm-thick transparent polystyrene plates (Kim *et al.*, 2015 and Lee *et al.*, 2018). The free-stream velocity (u_∞) can be varied from 0.01 to 3 m s^{-1}, and the turbulence

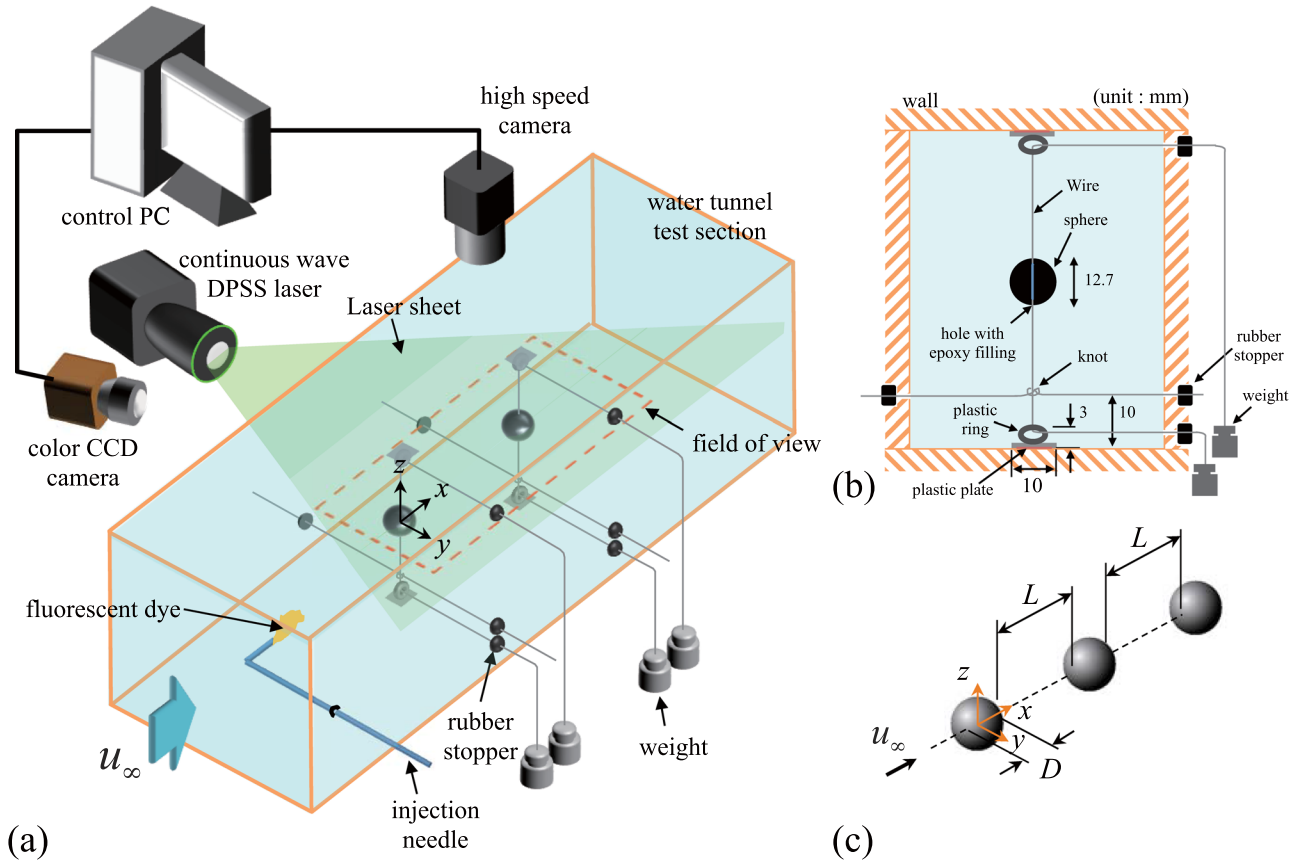

FIG. 1. Experimental setup for the particle image velocimetry measurement and dye visualization for the flow around a sphere array: (a) three-dimensional view; (b) cross-sectional view (orthogonal to the streamwise direction); (c) configuration of sphere array.

intensity is about 3.0% at 0.078 m s^{-1} of the free-stream velocity. The water-tunnel is equipped with one aluminum honeycomb and two stainless steel meshes placed upstream of the contraction pipe to make the flow straight and the turning vanes to make a smooth and efficient turn of a circulating flow around the corner. The contraction ratio is 7.6, while the contraction part is designed such that its profile is fitted with a third-order polynomial equation. All considered in-line sphere arrays are placed between 400 and 600 mm downstream of the test section inlet. For the spheres, we use steel bearing balls whose diameter is D = 12.7 mm, and the considered Reynolds number for a single sphere is $Re_D = u_\infty D/\nu = 1000$. Thus the blockage ratio (ratio of the sphere frontal area to the cross-sectional area of the test section) is about 2%, which is considered to have a negligible effect on the measurements (Achenbach, 1974). To locate each sphere at the exact positions required, it is firmly tethered by a 0.1 mm-thick stainless steel wire through a 0.2 mm-diameter hole that passes through the sphere from pole to pole (drilled using a dust-resistant technique). After the wire is made through, the hole is filled with an epoxy, and the details are illustrated in Fig. 1(b). To reduce the laser reflected on the sphere surface, it is colored black using a metal coloration that is found not to affect the condition of the sphere surface. After coloring, the diameter of spheres is measured at arbitrary points using a micrometer, which is 12.7 ± 0.005 mm (deviation within 0.04% from the pre-colored diameter). To construct an in-line sphere array, the number of spheres is varied from 1 to 5, and for each case, the spheres are equally spaced with a distance (L) from 0 to 3.0D [Fig. 1(c)].

For the in-line sphere array configuration, a small misalignment of a sphere against the flow direction would significantly alter the flow around it; thus, the location of each sphere needs to be precisely controlled. To ensure this, we employ a pulley system; that is, the vertical and lateral positions of a sphere are adjusted outside the test section by controlling the wires that are connected to the sphere through multiple rubber stoppers at the wall of the test section [Figs. 1(a) and 1(b)]. At each end of the wire, a weight is suspended to provide a sufficient tension to the threaded wire. The ring with a plate is positioned such that the laser sheet illuminating the field of view is not affected. To quantify the amount of possible misalignment, before each measurement set, the position of each sphere in the in-line array is measured with two cameras [Fig. 1(a)], and it is guaranteed that the deviated distance of a sphere center from the reference line does not exceed 0.4% of the sphere diameter for all the tested cases.

B. Particle image velocimetry and dye visualization

For particle image velocimetry measurements, plastic beads (Polyamid Particles, Dantec Dynamics) with a nominal diameter of 10 μm are seeded in the water tunnel. To illuminate the seeders, a 5 W continuous wave Nd:YAG laser (Ray-Power 5000, Dantec Dynamics) is used, whose wavelength is 532 nm. To capture the particle images, we use a high-speed camera (NX5, IDT) that can be operated at the speed of 500 Hz

with the resolution of 2560 × 1440 pixels. The conventional cross correlation based on Fourier transform is employed to evaluate the velocity vectors with a 32 × 32 pixel interrogation window (50% overlap). Spurious vectors are detected by the normalized median test (Westerweel and Scarano, 2005) and replaced with the mean value of the neighboring vectors in a 3 × 3 grid, when calculating the instantaneous velocity field. To obtain a fully converged flow field, more than 2000 instantaneous flow fields (obtained at the speed of 10 Hz by controlling the recording speed with a key macro program) are averaged for all the cases considered. Considering that the characteristic frequency of the present flow is about 1.2 Hz, this corresponds to more than 160 periods of vortex shedding. Thus, we believe that the statistical convergence of the time-averaged fields is guaranteed. The field of view has a range of $-0.6 \le x/D \le 6$–14.5 and $-1.5 \le y/D$ (or z/D) ≤ 1.5 with a spatial resolution of $0.067D$, and the center of the first sphere in each array is set to be the origin. The velocity measurements are mostly performed at the x–y plane that passes the centers of the spheres. On the other hand, to achieve the temporal resolution in measuring frequency characteristics of the flow, the size of the field of view is reduced to 300 × 300 pixels, and thus 20 000-30 000 instantaneous flow fields are obtained (including 40-60 periods of vortex shedding) at the speed of 500 Hz.

To support the results of velocity measurements on a two-dimensional plane, dye visualization is additionally performed to understand three-dimensional flow structures qualitatively. The green or orange colored fluorescent dye is injected through a thin needle at 100 mm (corresponding to 141 times the diameter of the needle) upstream of the first sphere. The injection needle is made of stainless steel (outer diameter of 0.71 mm), and its Reynolds number at the considered free-stream velocity is 55, where the wake behind a circular cylinder undergoes a transition from steady to unsteady ones (Taneda, 1956). We have confirmed that there is no perturbation in the wake behind a thin needle and also the flow around a sphere array is not affected. As a light source, we use UV lanterns (UVBe-100, UvBeast™) to illuminate the fluorescent dye, which are placed above the upper wall of the test section. At the side of the test section, a color CCD camera (VC-4MC, Viewworks) is positioned to capture the illuminated dye at 200 Hz, sufficiently faster than the characteristic frequency of the wake behind a single sphere (about 1.2 Hz) at the considered $Re_D = 1000$, with a resolution of 2048 × 1088 [Fig. 1(a)].

As the velocity component (u_{piv}) evaluated from the particle image can be expressed as $u_{piv} = M\Delta s/\Delta t$ (where M is the magnification factor, Δt is the time difference between evaluated particle images, and Δs is the particle displacement during the time duration of Δt), the uncertainty in evaluating u_{piv} can be estimated as Eq. (1) (Lawson *et al.*, 1999 and Kim *et al.*, 2015),

$$\delta(u_{piv}) = \sqrt{\delta(M)^2 + \delta(\Delta s)^2 + \delta(\Delta t)^2}. \quad (1)$$

Here, $\delta(\alpha)$ denotes the uncertainty in measuring α. In the present setup, the measurement error in the magnification factor is calculated as 0.42% with $M = 53.0$ μm/pixel. The inter-frame time interval was 1 μs, and thus the error involved in the time interval is estimated as 0.05%, where the time interval between the image pair is 2 ms. Finally, the resolution of the particle displacement is calculated as 3.8% with an average particle displacement of 3.0 pixel (Scarano, 2001). Thus the overall uncertainty is calculated to be about 3.8% for the present velocity measurement.

The flow around a single sphere is measured to test the validity of the present experimental setup. Shown in Fig. 2 are the wake characteristics behind a single sphere at $Re_D = 1000$. In particular, variations of mean streamwise velocity and streamwise turbulence intensity along the centerline are compared with those from previous studies at similar Reynolds numbers. We can see that the present data show a reasonable agreement with previous ones obtained from experimental and numerical approaches. In particular, the streamwise variation of the streamwise velocity and the consequent size of the recirculation bubble in the wake (highlighted with an arrow) match well with the previous studies [Fig. 2(a)]. The magnitude of the maximum streamwise turbulence intensity shows a slight difference among the compared data; however, the positions of local maximum and minimum turbulence intensity agree well with each other. Further validation is performed by measuring the Strouhal number ($St = fD/u_\infty$) of vortex shedding, based on the characteristic frequency (f) of the vertical velocity (v) measured at $2.5D$ downstream from the sphere center along the centerline. It is measured that the present St that characterizes the vortex shedding is about 0.2 [Fig. 2(c)], which agrees well with those reported by previous studies (Sakamoto and Haniu, 1990 and Tomboulides and Orszag, 2000).

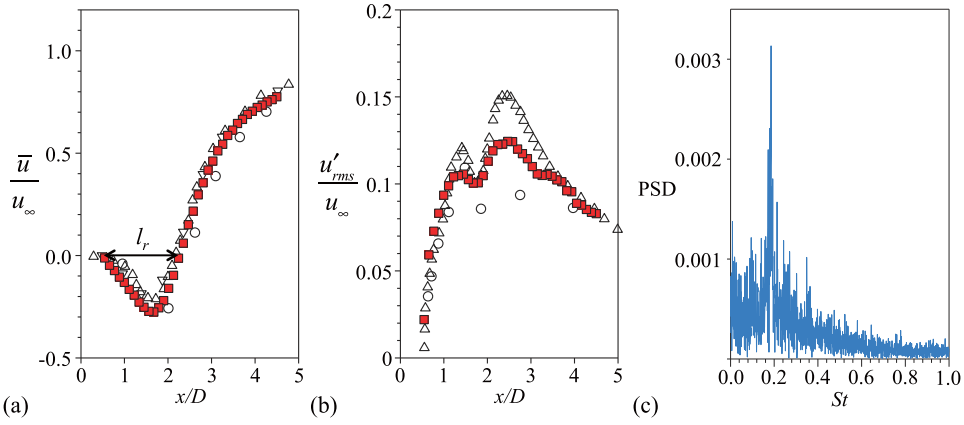

FIG. 2. Wake characteristics behind a single sphere at $Re_D = 1000$: (a) normalized mean streamwise velocity; (b) streamwise turbulence intensity along the centerline; (c) power spectral density (PSD) of the vertical velocity (v) measured at $x/D = 2.5$, $y/D = z/D = 0$. In (a) and (b), ■, present study ($Re_D = 1000$); △, Tomboulides and Orszag (2000) ($Re_D = 1000$); ▽, Wu and Faeth (1993) ($Re_D = 960$); ◯, Orr *et al.* (2015) ($Re_D = 1000$).

III. FLOW AROUND A SINGLE SPHERE AT Re_D = 1000

Before we discuss the flow around multiple spheres, the flow around a single sphere at $Re_D = 1000$ is explained in this section. Figure 3 shows a typical instantaneous flow structure obtained by dye visualization and particle image velocimetry. As shown in Fig. 3(a), a vortex tube evolves in the wake, which extends to the downstream about 1.0D from the rear end of a sphere. Along the vortex tube, the shear layer oscillates at the edges and this leads to the roll-up into a hairpin vortex [two legs and a head are highlighted in Fig. 3(a)]. This instability randomly occurs around the azimuthal positions on the vortex tube. While there are many previous reports on the wake behind a single sphere, according to Sakamoto and Haniu (1990), the vortex tube forms right behind the sphere and its pulsation generates a hairpin vortex periodically at $Re_D > 800$, which is also observed in the present measurement. This qualitative description of the flow is supported by the velocity distribution shown in Fig. 3(b), where the oscillation of the shear layer is clearly measured. Right behind the sphere, two shear layers with an opposite sign of vorticity develop along the streamwise direction, which is attributed to the aforementioned vortex tube. At $x/D \simeq 2.0$–2.5, the deflection of the shear layer occurs, indicating the existence of shear layer instability and the formation of wake vortices. The periodicity of this vortex shedding process has been reported in previous studies (Kim and Durbin, 1988; Sakamoto and Haniu, 1990; and Tomboulides and Orszag, 2000), and the present Strouhal number is measured to be $St \simeq 0.2$ (measured at $x/D = 2.5$, $y/D = z/D = 0$), agreeing with them. Although it is known that there exists another oscillation mode at a higher frequency corresponding to the shear-layer instability (Sakamoto and Haniu, 1990), it is not possible to capture it due to the insufficient temporal resolution and number of data in the present measurements.

Time-averaged flow fields measured on x–y and x–z planes are shown in Fig. 4. As shown, the distributions of mean velocity, vorticity, and turbulence intensity agree well with the

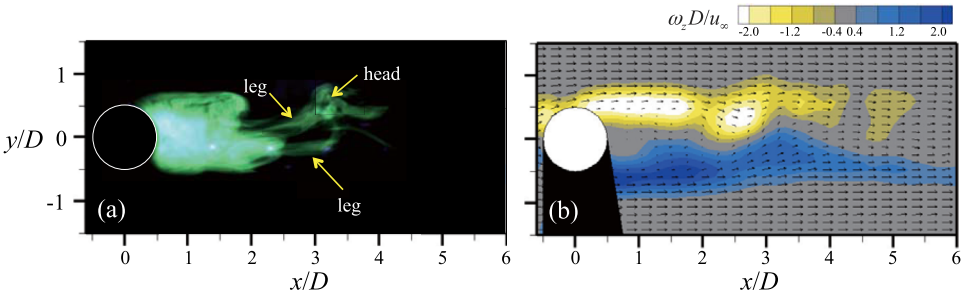

FIG. 3. Instantaneous flow structure around a sphere at $Re_D = 1000$: (a) dye visualization and (b) velocity vectors and vorticity ($\omega_z D/u_\infty$) contour.

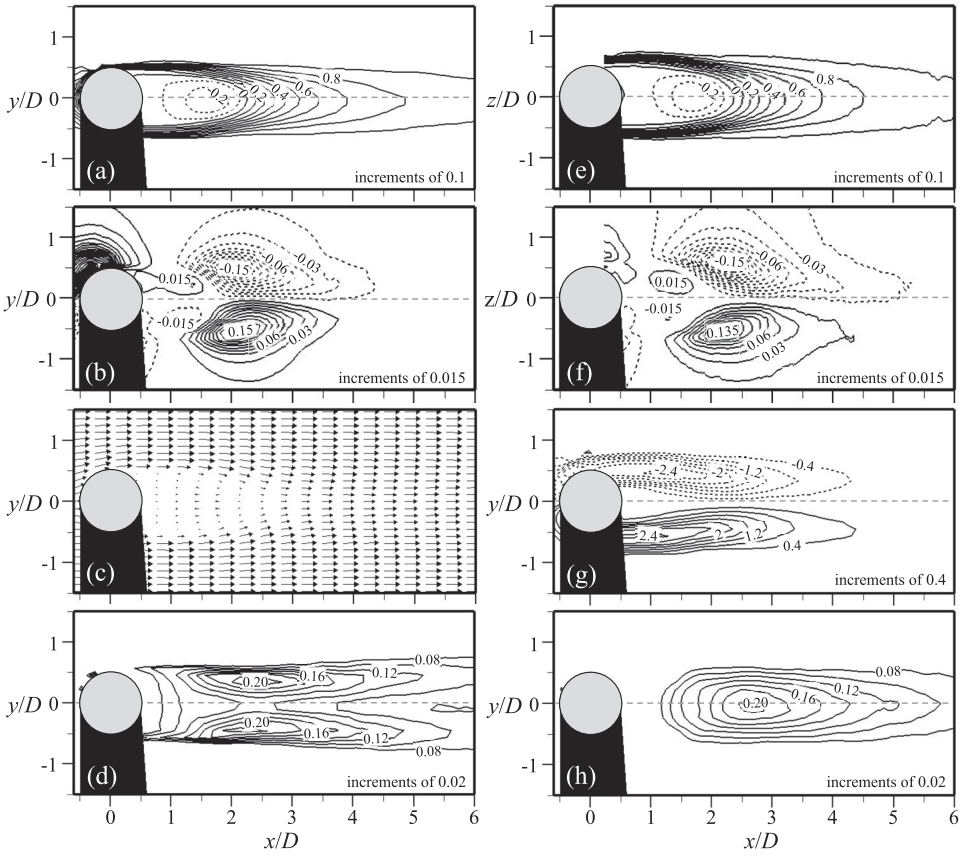

FIG. 4. Time-averaged flow around a single sphere at $Re_D = 1000$ in x–y [(a)–(d) and (g) and (h)] and x–z [(e) and (f)] planes: [(a) and (e)] streamwise velocity ($\bar{u}/u_\infty$); (b) vertical velocity ($\bar{v}/u_\infty$); (c) velocity vectors; (d) streamwise turbulence intensity (u'_{rms}/u_∞); (f) transverse velocity ($\bar{w}/u_\infty$); (g) transverse vorticity ($\omega_z D/u_\infty$); (h) vertical turbulence intensity (v'_{rms}/u_∞). In the contours, dashed lines denote negative values.

typical trends in the wake behind a sphere at a similar Reynolds number range. Strong shear layers develop behind the sphere [Fig. 4(g)], and its velocity gradient is quickly weakened near the vortex formation region [Figs. 4(c) and 4(g)]. In the present study, the size of the recirculation bubble (l_r) in the wake [i.e., streamwise distance to the position of zero mean streamwise velocity ($\bar{u} = 0$) from the sphere base] is measured to be $l_r/D = 1.76 \pm 0.07$. In previous studies, it was measured that $l_r/D = 1.7$ at $Re_D = 960$ (Wu and Faeth, 1993) and 1.71 at $Re_D = 1000$ (Tomboulides and Orszag, 2000). On the other hand, the streamwise turbulence intensity has two maximum peaks in the upper and lower shear layers (at $x/D = 2.2$, $y/D = \pm 0.4$) [Fig. 4(d)], which is attributed to the roll-up of shear layers (Fig. 3). It should be noted that two peaks are connected along the azimuthal direction, forming a circle that is orthogonal to the flow direction. The vertical turbulence intensity has a single maximum peak at $x/D = 2.7$, $y/D = 0$ [Fig. 4(h)]. Since the wake vortices from the shear layer roll-up contribute to the vertical velocity fluctuations mostly, the maximum v'_{rms} occurs slightly farther than that of u'_{rms}. To check the symmetry of the wake structure (and evaluate the effect of the holding wire, as well, see Sec. II A), we measure the velocity on the x–z plane and confirm that the exactly same flow fields are measured [Figs. 4(e) and 4(f)]. Thus, we believe that the thin wire that holds the sphere has a negligible influence on the flow measurements, and the flow around a single sphere at the present Reynolds number is statistically axisymmetric, agreeing with the previous studies (Mittal *et al.*, 2002). Based on this instantaneous and time-averaged flow fields behind a single sphere, as a reference condition, we will discuss the effects of the additional sphere on the flow while varying the number of spheres and the distance between them.

IV. FLOW AROUND IN-LINE SPHERE ARRAY

A. Flow around a two-sphere array

Figure 5 shows the representative instantaneous flow visualization and velocity (vorticity) distribution for a two-sphere array with the spacing of $L/D = 0.33$ and 1.0. When the second sphere is placed behind the leading sphere in proximity, obviously it affects the wake structure behind the leading one and it is also under the influence of the non-uniform incoming flow. If the spacing between two spheres is $L/D \leq 0.33$, the trailing sphere is entirely inside the recirculation region behind the leading sphere, while the wake behind the leading sphere remains to be axisymmetric, but no specific frequency in the flow is measured [Figs. 5(a)–5(d)]. Behind the trailing sphere, the shedding of hairpin vortices is captured, similar to the wake behind a single sphere. In Figs. 5(a) and 5(b), which were taken successively on the x–y plane, the process of the hairpin vortex shedding is shown (see the arrows in the figures) and the same phenomenon is observed on the x–z

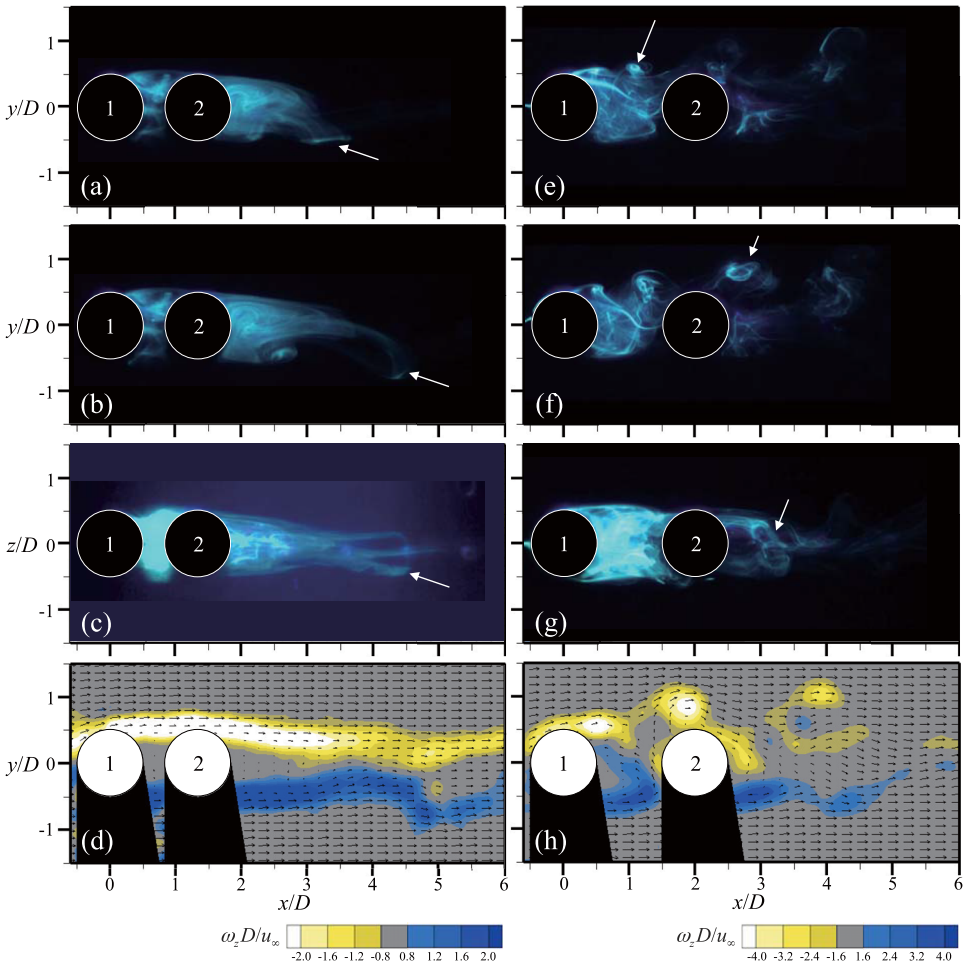

FIG. 5. Instantaneous flow around a two-sphere array with $L/D = 0.33$ [(a)–(d)] and 1.0 [(e)–(h)]: dye visualization on x–y [(a), (b), (e), and (f)] and x–z [(c) and (g)] planes; [(d) and (h)] vorticity ($\omega_z D/u_\infty$) and velocity distribution on the x–y plane.

plane as well [Fig. 5(c)]. That is, the hairpin vortex starts to shed from the vortex loop attached to the rear end of the trailing sphere and flows downstream, while new one emerges from the vortex loop. Unlike the single sphere wake, however, the wake behind a trailing sphere is planar symmetric. The instantaneous velocity field for $L/D = 0.33$ is shown in Fig. 5(d), where the separating shear layer from a leading sphere is connected to that from the trailing sphere without being deflected. Behind the second sphere, the instability of a separating shear layer is observed at about $1.5D$ away from the rear end, which is earlier than that (about 2.0–2.5D) of a single sphere case. The characteristic Strouhal number for the wake behind the trailing sphere is measured to be about 0.2, the same as the single sphere wake.

When the spacing between two spheres increases to $1.0D$, the wake behind a leading sphere deforms to shed unsteady vortices, resulting in a biased gap flow [Figs. 5(e)–5(h)]. Unlike the wake of an isolated sphere, the generation of vortex in the first wake dominantly takes place in one azimuthal direction, i.e., at the upper part of the wake when viewed from the x–y plane [see the arrows in Figs. 5(e) and 5(f)], while the vortex shedding in the other directions seldom occurs. The characteristic frequency for this vortex structure in the gap is measured to be relatively high as $St = 0.45$ (at $x/D = 1.4$, $y/D = 0.5$). While the orientation of the gap flow in the present condition is directed upward in the x–y plane, we find that it is sensitive to the alignment of a trailing sphere with respect to the flow direction. That is, even a very slight movement of the trailing sphere (less than 1 mm) incurs the change in the direction of shed vortices; however, like the case of $L/D = 0.33$, it is not possible to establish the condition to make the first wake to be axisymmetric. The asymmetric wake from the first sphere significantly affects the wake of a trailing sphere. As shown in Figs. 5(e)–5(g), it is hard to elucidate the second wake structure from dye visualization, indicating that it is highly dissipative, compared to that of $L/D = 0.33$. In the instantaneous velocity field, on the other hand, the interaction between the first and second wake flows can be observed [Fig. 5(h)]. That is, the strongly biased first wake (toward the upper shear layer) induces a downward flow in the second wake, which seems to further prevent the evolution of the upper shear layer from the trailing sphere. At the lower part, on the other hand, more regular shear layers evolve, and thus it is classified that the overall flow structure around the two-sphere array ($L/D = 1.0$) is planar symmetric. As will be discussed later, on the other hand, it is better to classify the wake of the second sphere as the transition from an asymmetric to axisymmetric flow structure, when judged from the velocity and turbulence intensity distributions together.

This interpretation of the flow is supported by the time-averaged flow fields on the x–y plane for $L/D = 0.33$ and 1.0 [Figs. 6 and 7]. As we have explained with instantaneous flow fields, the flow in the x–y plane shows the asymmetric distribution, but it is symmetric in the x–z plane (not shown here), indicating that the flow is planar symmetric. For the case of $L/D = 0.33$, a very strong shear layer is generated from the leading sphere, but the flow in the gap is nearly stagnant, although the fluid in that region actually circulates around the vortex core [Figs. 6(a) and 6(b)]. For the trailing sphere, the wake defect region is reduced compared to that of a single sphere wake [Fig. 7(a)]. Since the convection of the wake vortices is oriented to one azimuthal direction [strong negative $\bar{v}$ in Fig. 7(b)], the asymmetric distribution of turbulence intensity is measured, in which the local maximum occurs at the lower part where the head of the hairpin vortex shows up, flows out, and dissipates along the streamwise direction [Figs. 7(c) and 7(d)]. In a time-averaged sense, this asymmetric wake flow will induce a side force on the sphere along the positive y-direction because the hairpin vortices constantly accelerate the surrounding fluid downwards, and this is quite similar to the wake structure behind a rising bubble [at $Re_D > \boldsymbol{O}(10^2)$] that induces its path instability (Magnaudet and Mougin, 2007 and Lee and Park, 2017). As the spacing increases to $L/D = 1.0$, the first wake has a strong upward gap flow [Fig. 7(f)], which has a negative streamwise velocity [Figs. 6(c) and 7(e)]. A strong streamwise turbulence is generated along the upper part of this gap flow [Fig. 7(g)], which is attributed to the energetic roll up of the vortices occurring there [Figs. 5(e) and 5(f)]. In the gap, on the other hand, the streamwise turbulence intensity is not strong [Fig. 7(g)], but the vertical component is rather strong and has the local maximum near the stagnation point of a trailing sphere [Fig. 7(h)]. This is because the hairpin vortex from the upper shear layer of a leading sphere consistently interacts with the trailing sphere, leading to a rapid

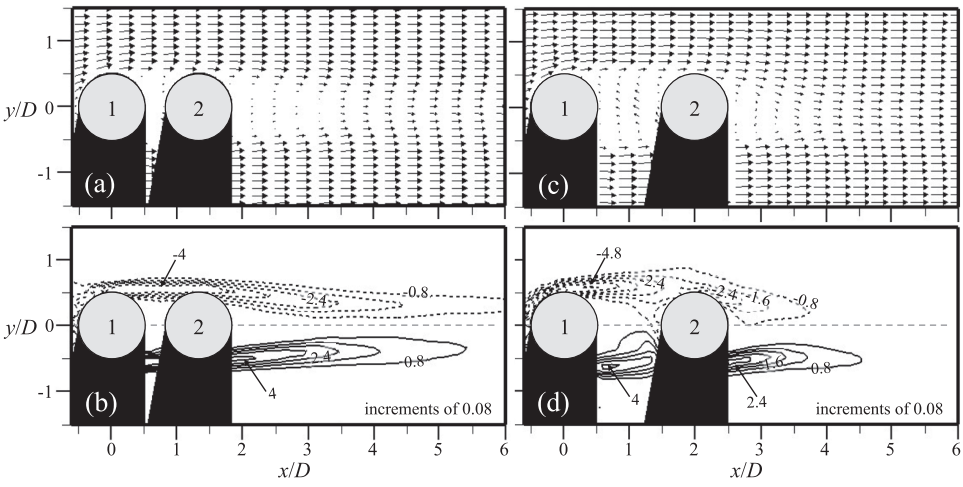

FIG. 6. Time-averaged flow around a two-sphere array with $L/D = 0.33$ [(a) and (b)] and 1.0 [(c) and (d)]: [(a) and (c)] velocity vector field; [(b) and (d)] transverse vorticity ($\omega_z D/u_\infty$). In the contours, dashed lines denote negative values.

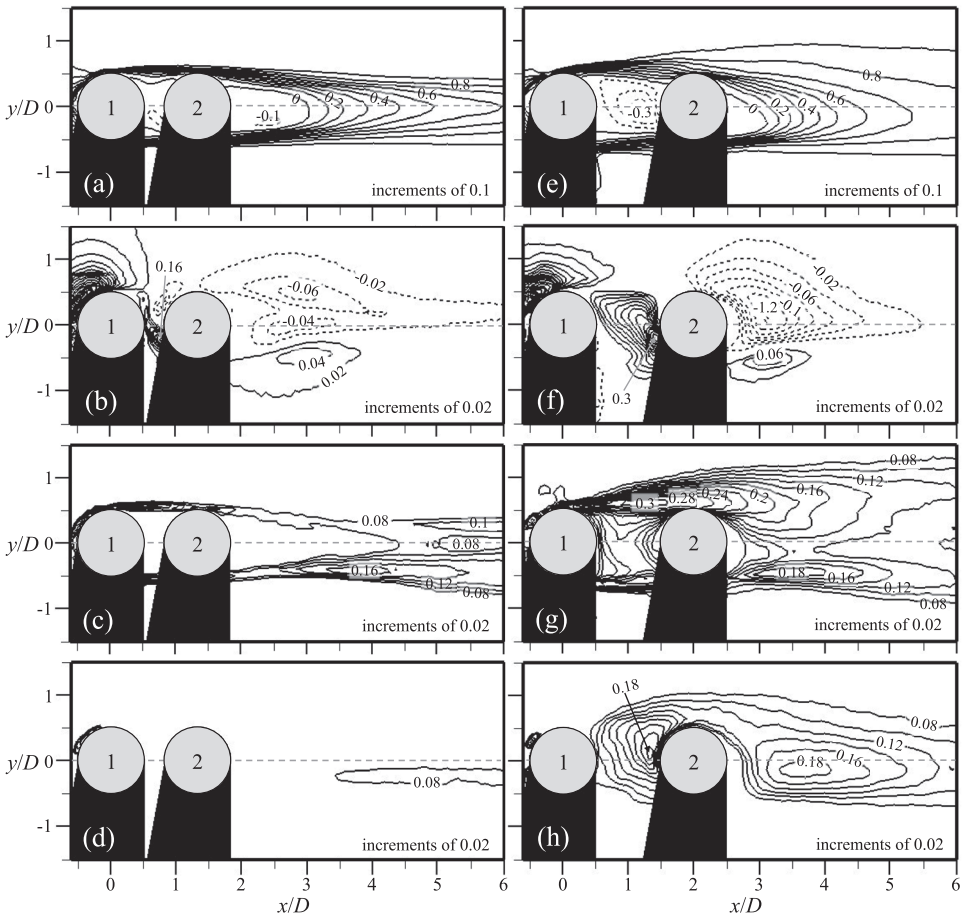

FIG. 7. Time-averaged flow around a two-sphere array with L/D = 0.33 [(a)–(d)] and 1.0 [(e)–(h)]: [(a) and (e)] streamwise velocity ($\bar{u}/u_\infty$); [(b) and (f)] vertical velocity ($\bar{v}/u_\infty$); [(c) and (g)] streamwise turbulence intensity (u'_{rms}/u_∞); [(d) and (h)] vertical turbulence intensity (v'_{rms}/u_∞). In the contours, dashed lines denote negative values.

eruption near the frontal part. For the present Reynolds number, the size of the recirculation bubble in the wake was about 1.76D and the shear-layer roll-up occurs at $x/D \simeq 1.0$ [Figs. 2 and 3]. At $L/D < 1.0$, thus the quasi-steady gap flow is induced. However, at this moderate spacing of $L/D = 1.0$, the instability of the shear layer separated from the leading sphere is directly perturbed by the trailing sphere. Thus, the roll-up vortex (i.e., hairpin vortex) is pushed upward by the trailing sphere, and the legs of the hairpin vortex are stretched, which creates a strong upward flow in the gap. Figures 7(f) and 7(h) show that this upward flow is initiated from the beginning of the upper shear layer and triggers a new hairpin vortex [Fig. 7(f)]. This self-trigger process seems to maintain constant shedding direction and cause the asymmetry. As L/D increases further, the trailing sphere will not affect the shear-layer roll-up and the flow axisymmetry tends to be recovered (see below). Past the trailing sphere, the slightly tilted-down flow and the skewed wake profile are observed [Fig. 6(c)], which leads to the thinning (thickening) of the lower (upper) shear layer [Fig. 6(d)]. As the dye visualization has shown, this consequently leads to the suppression (promotion) of the vortex roll-up in the lower (upper) shear layers, respectively, which results in the increase in a relatively strong turbulence intensity toward the upper part of the second wake [Figs. 7(g) and 7(h)].

When two spheres are displaced with a spacing of 2.0D and 3.0D, the overall shape of the wake (mean velocity and turbulence intensity) of a leading sphere recovers the flow structures similar to the single sphere wake (not affected much by the presence of a trailing sphere), but the second wake is still under the influence of the first wake [Figs. 8 and 9]. Figure 8 shows the time-averaged flow fields for the case of $L/D = 2.0$. Compared to the smaller spacing of $L/D \leq 1.0$, now the symmetry between upper and lower shear layers has been recovered. The strong shear layers evolve at both sides of the first wake, and a backflow is induced in the gap [Figs. 8(a) and 8(d)]; however, the recirculation region is not fully closed [Fig. 8(b)]. Along the vertical (y) direction at $x/D \simeq 2.0$–2.5 in the first wake, there are two positions of local maximum of streamwise (vertical) turbulence intensity [Figs. 8(e) and 8(f)], of which the level is comparable to the single sphere wake. The Strouhal number of the first sphere wake is measured to be 0.17 and 0.24 in the shear layer and gap, respectively, not much different from the single sphere wake. Despite this similarity, the maximum peak of streamwise turbulence intensity is located slightly farther away from the centerline ($y/D = 0$) than the single sphere wake, and there is a valley in the contour of vertical turbulent intensity (at $x/D = 1.5$–2.0). This is because the evolution of the separating shear layer from the first sphere is interfered by the second sphere, by which they bend to both sides of the second sphere and smoothly connect to the separating shear layers past the second sphere [Fig. 8(d)]. As a result, an early vortex roll-up is forced in the separating shear layer from the second sphere and the size of its recirculation bubble is reduced much ($l_r \simeq 0.47D$), while the maximum peak of the turbulence intensity locates closer to the base of the

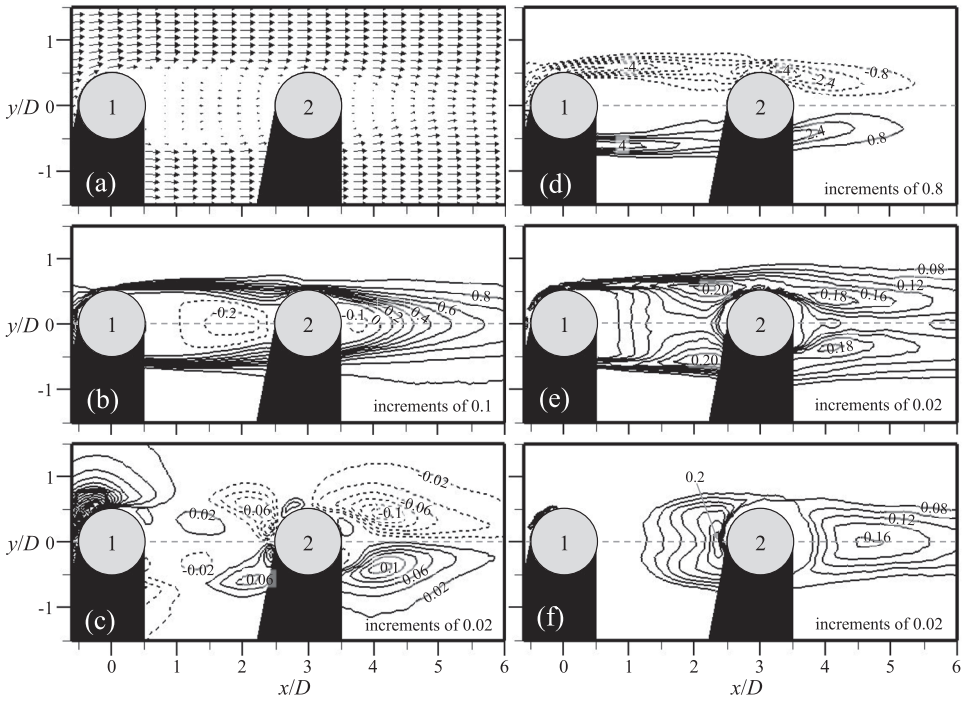

FIG. 8. Time-averaged flow around a two-sphere array with L/D = 2.0: (a) velocity vector field; (b) streamwise velocity ($\bar{u}/u_\infty$); (c) vertical velocity ($\bar{v}/u_\infty$); (d) transverse vorticity ($\omega_z D/u_\infty$); (e) streamwise turbulence intensity (u'_{rms}/u_∞); (f) vertical turbulence intensity (v'_{rms}/u_∞). In the contours, dashed lines denote negative values.

second sphere [Figs. 8(e) and 8(f)]. As the flow passes the second sphere, the turbulence intensity level decreases slightly, and the Strouhal number of the second wake is measured to be St = 0.17–0.24. When the spacing between two spheres is larger than 2.0D, the shear layer of the first wake sheds hairpin vortices in a random azimuthal direction [Fig. 9(a)], equivalent to the single sphere wake. Still, the trailing sphere is affected by the wake of a leading sphere such that the vortex roll-up process on the shear layer is encouraged to occur earlier. Thus, both the upper and lower shear layers are shortened by the wake of a leading sphere [Fig. 9(b)].

Figure 10 shows the L/D-dependency of the recirculation length (l_r) and Strouhal number (St) of the wake behind each sphere in a two-sphere array, being compared to those of a single sphere wake. We measure St at two vertical positions of y/D = 0 and 0.5 at 1.4D downstream of each sphere center, which characterizes the dynamics of gap and shear layer flows, respectively. It is found that the recirculation length of a leading sphere is directly determined (i.e., being linearly proportional to) by the spacing up to $L/D \simeq 2.0$ and then saturates to the value of a single sphere wake (being independent of L/D) at $L/D > 2.0$ [Fig. 10(a)]. As we have shown, this is because the second sphere is located inside the recirculation bubble behind the first sphere at $L/D < 2.0$. In terms of the characteristic frequency, the wake structures are also altered according to L/D. When the spheres are very close to each other ($L/D \lesssim 0.33$), the flow in the gap (standing vortex) is steady, while the shear layer bordering the edge of the gap flow is weakly perturbed by the shear-layer instability (but no dominant frequency is captured) [Fig. 10(b)]. At L/D = 1.0 where the significant asymmetry in the first wake has been observed, the salient periodic wave is detected, while the corresponding Strouhal number increases to 0.1 and 0.45 in the gap and shear layer, respectively. As we have explained, this is caused by the asymmetric generation (into the positive y-direction in the present condition) of the hairpin vortex. As L/D increases further to 2.0, both in the gap and shear layer, there exists an evident fluctuating signal ($St \simeq 0.2$ that is the same as the single sphere wake). When the spacing is larger than 3.0D, both Strouhal numbers in the shear layer and gap level off to the value of a single sphere. Unlike the first sphere wake, the St of the second sphere remains to be relatively constant (same as the single sphere) with varying L/D, but l_r of the second sphere varies with L/D. l_r decreases with increasing L/D (up to 1.0), reaching the minimum, and recovers the initial value with a further increase in L/D; however, it is still smaller than that of the single sphere [Fig. 10(a)], which is attributed to the fact that the increased turbulence level in the flow before the

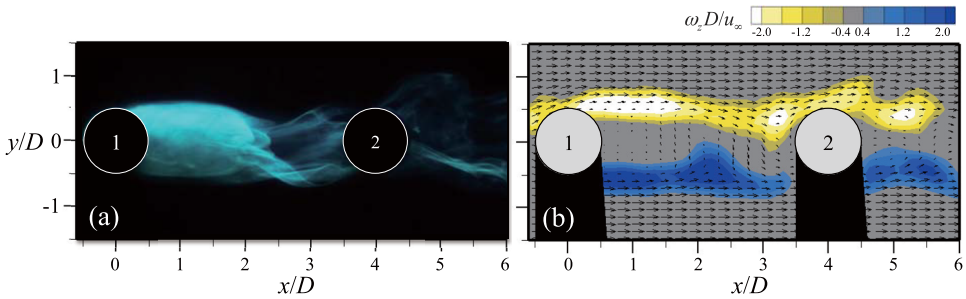

FIG. 9. Instantaneous flow around a two-sphere array with L/D = 3.0: (a) dye visualization and (b) velocity vectors and vorticity ($\omega_z D/u_\infty$) contour.

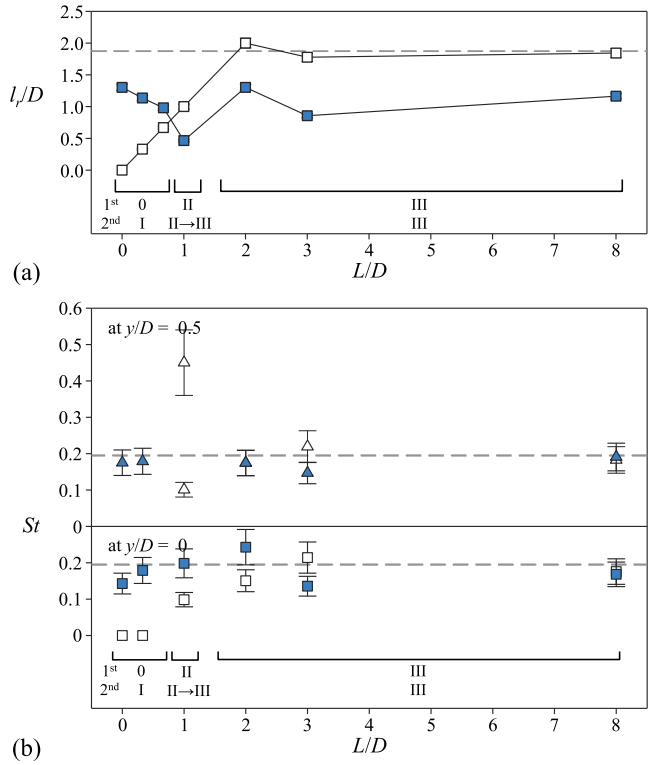

FIG. 10. Wake characteristics of a two-sphere array with L/D: (a) recirculation length (l_r): □, first wake; ■, second wake. (b) Strouhal number (St) at the shear layer (△, y/D = 0.5) and the gap (□, y/D = 0), measured at x/D = 1.4: open symbols, first wake; closed symbols, second wake. In the figures, dashed lines denote the case of a single sphere wake.

second sphere will encourage the early roll-up of the separating shear layer (Roshko, 1955; Gerrard, 1966; and Bagchi and Balachandar, 2004). When the spacing is larger than 3.0D, the recirculation length tends to increase slowly, and thus it is expected that the single sphere value will be achieved at a much larger L/D (e.g., $L/D > 10.0$).

In Fig. 10, based on the changes in the wake structures being supported by the variations of l_r and St, we identify four regimes for the flow around a two-sphere array, depending on L/D. When $L/D \leq 0.33$, the first wake includes a trailing sphere and is steady (regime 0). At this condition, the second wake is characterized by planar symmetric hairpin vortices [Figs. 5(a)–5(d)] with the same St as a single sphere wake. The turbulence level in the second wake is smaller than that of a single sphere. This is classified as regime I. When the spacing becomes larger ($L/D \gtrsim 2.0$), both wakes show the same structures with hairpin vortices as the single sphere wake, i.e., axisymmetric and $St \simeq 0.2$ both in the gap and shear layer (regime III). While the wake structures are similar, the recirculation length is shorter due to early shear layer roll-up in the second wake, indicating a different drag force on each sphere. When L/D = 1.0, the first wake has an asymmetric gap flow (oscillating at a lower frequency of $St \simeq 0.1$), and the hairpin vortices are actively generated at one azimuthal direction [Figs. 5(e)–5(h)] at a higher frequency of $St \simeq 0.45$, which leads to a stronger turbulence than a single sphere wake. This wake is termed as regime II. The second wake (at L/D = 1.0) experiences a slight asymmetry, e.g., the dominant downward velocity in the wake, and is classified as a transition stage from an asymmetric (regime II) to an axisymmetric (regime III) flow.

B. Flow around a multiple-sphere array

In Secs. III and IV A, we have discussed that the wake behind a sphere is significantly affected by the additional sphere located nearby, in terms of the flow symmetry, turbulence intensity, and Strouhal number. Thus, in this section, we further our understandings by investigating the flow modification due to multiple (more than three) spheres, according to the number of spheres and spacing (L/D) between them. Our focus will be on the above three properties of the wake structure.

1. Change in the flow symmetry

Figure 11 shows the dye visualization of the flow around a multiple-sphere array for the spacing of L/D = 0.33 on the x–y plane. Similar to the two-sphere array, standing (also axisymmetric) vortices show up in the gap between the spheres, while small perturbation exists on the shear layer. In the wake behind the last sphere, the vortex tube elongates along the streamwise direction about 1.0D from the base of the last sphere and evolves into planar hairpin vortices (with a head directed downward, highlighted with arrows in the figure) periodically at the frequency of St = 0.2. The planar symmetry of the flow at this condition is confirmed by the velocity measurements on the x–z plane, which is perpendicular to the symmetry plane (Fig. 12). When the spacing is 0D [Figs. 12(a) and 12(b)]

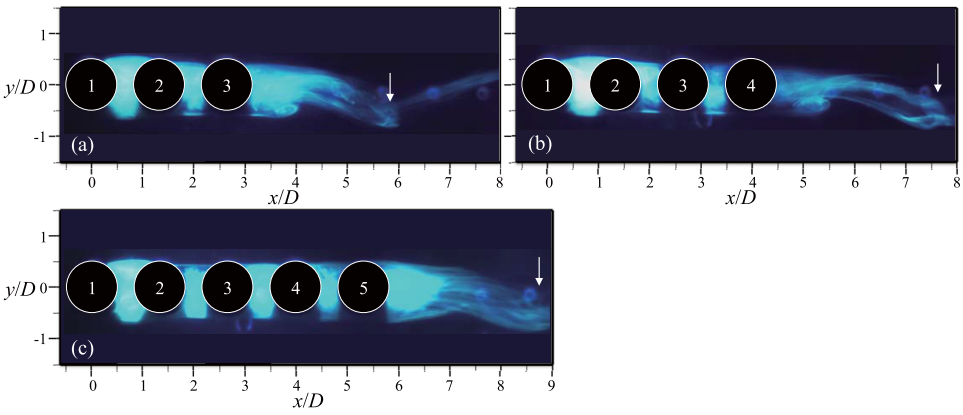

FIG. 11. Dye visualization of the flow around a multiple sphere array with L/D = 0.33: (a) three-sphere array; (b) four-sphere array; (c) five-sphere array.

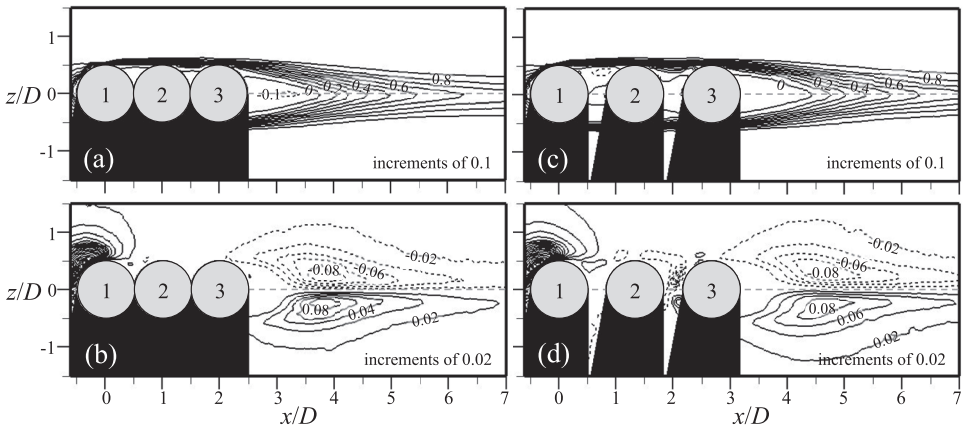

FIG. 12. Time-averaged flow around a three-sphere array with [(a) and (b)] L/D = 0 and [(c) and (d)] 0.33: [(a) and (c)] streamwise velocity ($\bar{u}/u_\infty$); [(b) and (d)] transverse velocity ($\bar{w}/u_\infty$). In the contours, dashed lines denote negative values.

and 0.33D [Figs. 12(c) and 12(d)], we can see that the time-averaged velocity distributions show a symmetric trend against the plane of $z/D = 0$. The same flow fields are measured even with a further increase in the number of spheres.

The dye visualization and velocity measurement on x–y and x–z planes of the four-sphere array with the spacing of L/D = 1.0 are shown in Fig. 13. The planar symmetric hairpin vortices dominantly shed from the upper shear layer of the first wake (highlighted with head-filled arrows) and move along the upper side of the rest spheres in the array, which is the same as the first wake of a two-sphere array [Figs. 13(a) and 13(b)]. The interaction between this hairpin vortex and trailing spheres is observed in the velocity (vorticity) field, and the strong gap flow along the upward direction is induced in the first wake [Fig. 13(d)]. At the second wake, planar hairpin vortex shedding dominantly occurs at the lower shear layer due to the non-uniform inflow to the second sphere. Behind the third sphere in the four-sphere array, unlike the first wake, the roll-up of the shear layer into vortices shows up in random directions. For example, in Figs. 13(b) and 13(e), the generation of the hairpin vortex from the shear layer along the negative z-direction (indicated by the line-head arrows) is detected. Due to this random direction of vortex roll-up, the planar symmetry in the wake is broken from the third wake. Figure 14 shows the flow statistics around a three-sphere array on x–y and x–z planes, for a spacing of L/D = 1.0. While the flow is asymmetric on the x–y plane, the symmetry of the flow is measured on the x–z plane (against the $z = 0$ plane), indicating that the flow is statistically planar symmetric. In the first gap, a strong upward flow is induced, indicating a biased vortex generation in the gap [Fig. 14(b)], and these strong shed vortices would significantly affect the following wakes such that the downward flow is induced in the second gap, but the flow symmetry is recovered in the third wake. When L/D = 1.0, it is found that the third (last) wake is an axisymmetric flow. Figure 15 compares the profiles of time-averaged velocity and turbulence intensity along the streamwise direction in the third wake of a three-sphere array (L/D = 1.0), measured on x–y and x–z planes. As shown, the velocity profiles agree well with each other, supporting our understanding that the last wake of the three-sphere array with L/D = 1.0 is axisymmetric. On the other hand, the streamwise turbulence intensity on the x–y plane at

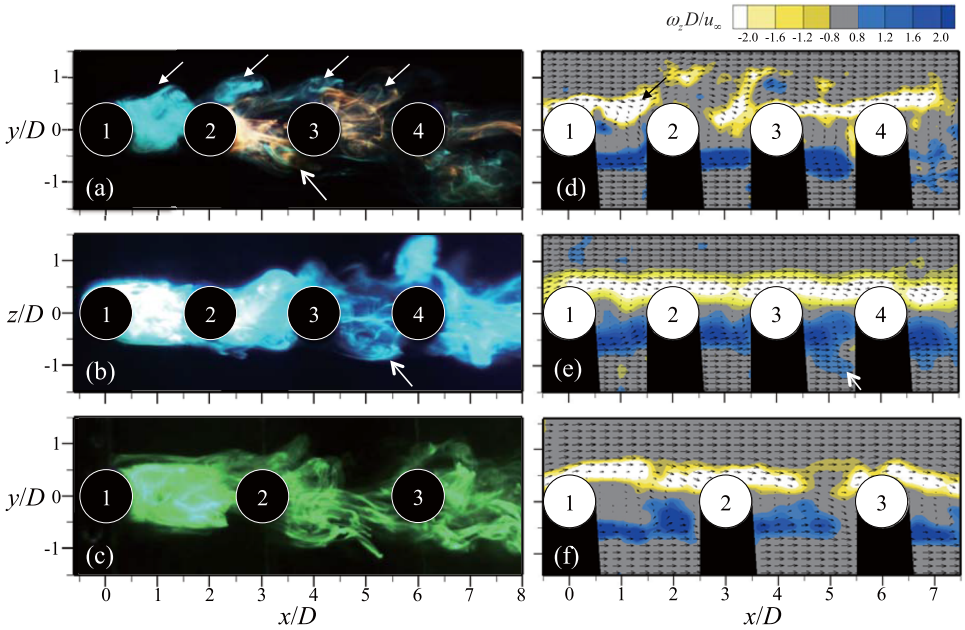

FIG. 13. Instantaneous flow around a multiple-sphere array: [(a), (b), (d), and (e)] four-sphere array with L/D = 1.0; [(c) and (f)] five-sphere array with L/D = 2.0: [(a)–(c)] dye visualization; [(d)–(f)] vorticity ($\omega_z D/u_\infty$) and velocity distribution.

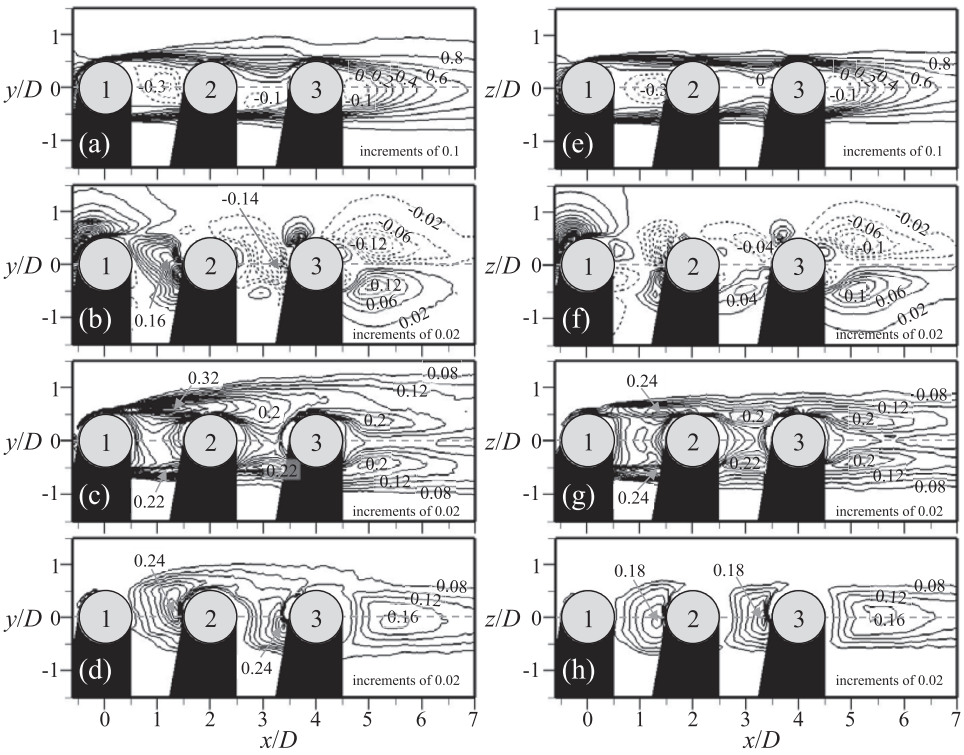

FIG. 14. Time-averaged flow around a three-sphere array with L/D = 1.0: [(a) and (e)] streamwise velocity ($\bar{u}/u_\infty$); [(b) and (f)] vertical and transverse velocity ($\bar{v}/u_\infty$; $\bar{w}/u_\infty$); [(c) and (g)] streamwise turbulence intensity (u'_{rms}/u_∞); [(d) and (h)] vertical and transverse turbulence intensity (v'_{rms}/u_∞; w'_{rms}/u_∞). In the contours, dashed lines denote negative values.

$y/D > 0.5$ is slightly larger than that on the x–z plane due to the presence of the convecting hairpin vortices mainly generated from the upward shear layer of the first wake. Despite this, it is interesting to observe that the global axisymmetry of the third wake is maintained and this remains further even if an additional sphere is located behind the three-sphere array with L/D = 1.0.

When the spacing between each sphere becomes as large as 2.0D, the shear layers from all spheres in the array are evolved into hairpin vortices oriented in random directions [see Figs. 13(c) and 13(f), for example]. The first sphere sheds the hairpin vortices with a specific frequency of St = 0.15 (in the gap), and these vortices affect the second sphere wake, leading to shortened and disrupted shear layers of the following sphere wakes [Fig. 13(f)] with the frequency of St = 0.24 (in the gap). Despite the random shedding direction of hairpin vortices in the instantaneous flow, Fig. 16 shows that the flow around a five-sphere array is statistically symmetric on the x–y plane. The same flow structures are measured on the x–z plane (not shown here), indicating that the flow is axisymmetric. The size of the recirculation bubble in the wake is drastically reduced from the first to the second wake, slightly increases in the third wake, and seems to converge from it. The turbulence intensity level in the wake is similar for all sphere wakes except the first wake, to which the inflow is uniform and has a very low level of turbulence.

2. Modulation of turbulence intensity

Figure 17 shows the variation of turbulence intensity profiles along the streamwise location for the two-to-five sphere arrays with a spacing of L/D = 0, whose flow structure is planar symmetric. Note that measurement is taken on the symmetry plane (x–y plane). In the gaps between spheres (x/D = 0.5, 1.5, 2.5, and 3.5), locally enhanced velocity fluctuation (perturbation) is measured along the shear layer (y/D = 0.5), as we have visualized above. This perturbation dominantly oscillates in the streamwise direction [Fig. 17(a)] compared to the vertical direction [Fig. 17(b)]. In the last wake of each sphere array (x/D = 2.0, 3.0, 4.0, and 5.0), both streamwise and vertical turbulence intensity profiles are symmetric to the centerline (y/D = 0) and has two maxima on the upper and lower shear layers. The magnitude of these peaks is about half of the single sphere case, while it is almost constant regardless of the number of spheres.

As the distance between the spheres increases to 1.0D, the separating shear layers in the wake of all spheres are

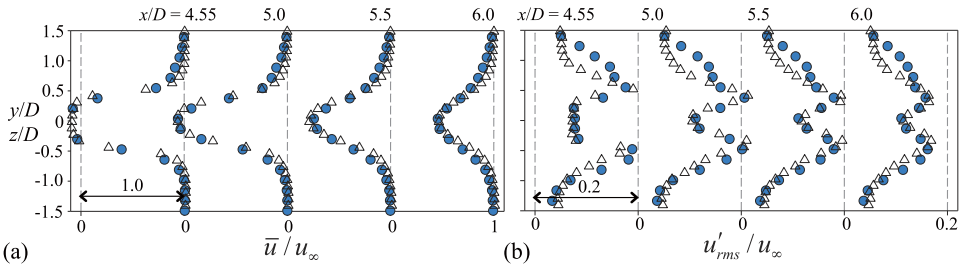

FIG. 15. Velocity profiles in the wake behind the last sphere in a three-sphere array measured on x–y (●) and x–z (△) planes: (a) mean streamwise velocity ($\bar{u}/u_\infty$) and (b) streamwise turbulence intensity (u'_{rms}/u_∞).

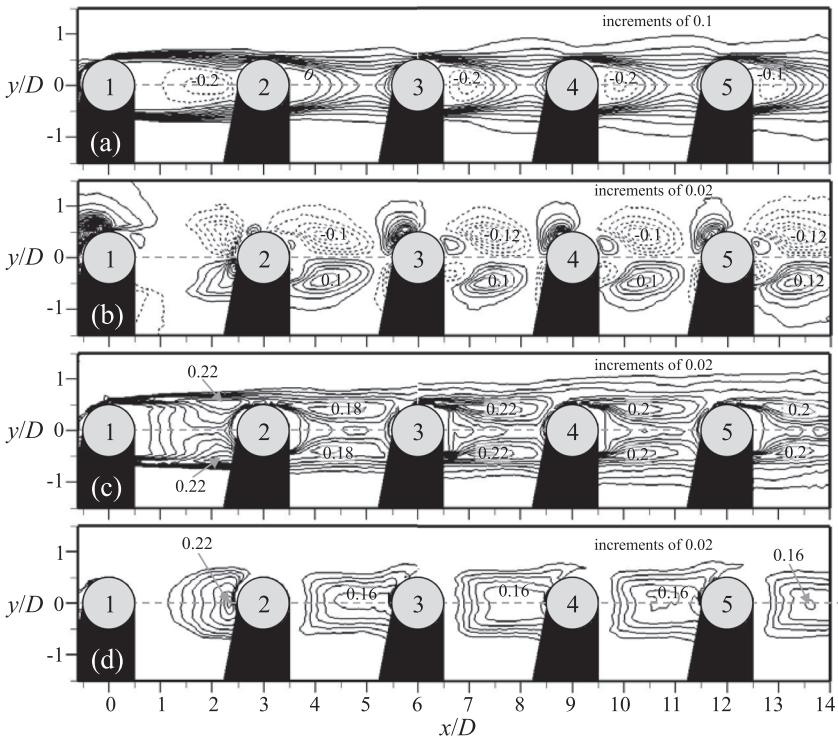

FIG. 16. Time-averaged flow around a five-sphere array with L/D = 2.0: (a) streamwise velocity ($\bar{u}/u_\infty$); (b) vertical velocity ($\bar{v}/u_\infty$); (c) streamwise turbulence intensity (u'_{rms}/u_∞); (d) vertical turbulence intensity (v'_{rms}/u_∞). In the contours, dashed lines denote negative values.

unstable and thus have a relatively higher level of turbulence intensity (Fig. 18). The first wake (x/D = 1.0) has a stronger turbulence level on the upper shear layer than on the lower one, which is also greater than that of a single sphere wake. This is again due to the energetic shedding of hairpin vortices biased toward the upper direction in the first gap. From the second wake ($x/D \geq 3.0$), however, the maximum value of the streamwise turbulence intensity at upper and lower shear layers

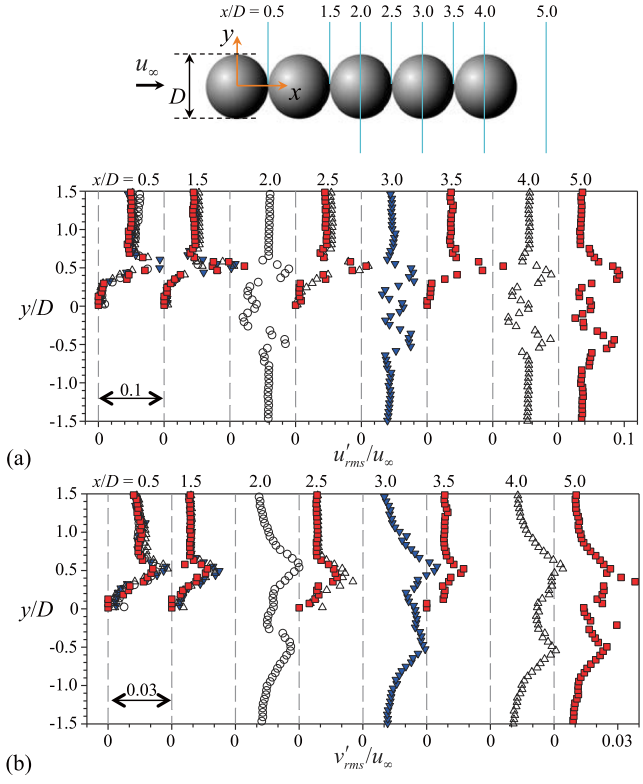

FIG. 17. Turbulence intensity profiles (in the middle of the gap and 1.0D away from the center of the last sphere) in a sphere array with L/D = 0: (a) streamwise turbulence intensity (u'_{rms}/u_∞) and (b) vertical turbulence intensity (v'_{rms}/u_∞). ◯, two-sphere array; ▼, three-sphere array; △, four-sphere array; ■, five-sphere array.

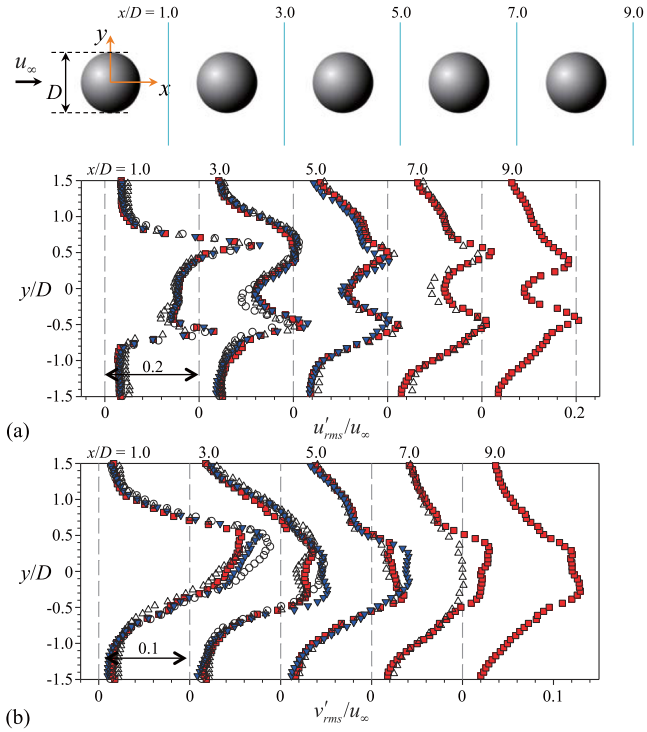

FIG. 18. Turbulence intensity profiles (1.0D away from the sphere center) in a sphere array with L/D = 1.0: (a) streamwise turbulence intensity (u'_{rms}/u_∞) and (b) vertical turbulence intensity (v'_{rms}/u_∞). ◯, two-sphere array; ▼, three-sphere array; △, four-sphere array; ■, five-sphere array.

becomes similar, and the shape of the profile also changes to a symmetric one [Fig. 18(a)]. In each wake, the vertical turbulence intensity is symmetric [Fig. 18(b)] and its magnitude becomes similar to that of a single sphere wake. Previously, Bagchi and Balachandar (2004) simulated the flow around a sphere ($Re_D = 610$) under various free-stream turbulence levels ($u'_{rms}/u_\infty = 0.1$–0.25) and reported that weak turbulence in the free-stream promotes vortex formation in the wake, but strong turbulence interferes with the vortex shedding process. Thus the convergence of the sphere wake is thought to be the result of the interaction between the trailing sphere wake and the turbulence in the leading sphere wake. It is noted that the turbulence intensity of the last wake of a four-sphere array is slightly weaker than that of the fourth wake of a five-sphere array ($x/D = 7.0$) (Fig. 18). When the trailing sphere exists inside the recirculation region of the leading sphere, the separating shear layer from the leading one re-attaches to the next sphere, forming an oscillating gap flow. In the gap flow, thus much stronger vorticity is accumulated until the shedding occurs, which results in the enhanced turbulence with a trailing sphere.

The streamwise and vertical turbulence intensity profiles in the wake behind each sphere of two-to-five sphere arrays with $L/D = 2.0$ are shown in Fig. 19. As shown, two distinct peaks appear in each wake and the profiles are symmetric against the $y = 0$ plane, which is very similar to that of a single sphere wake. Interestingly, the turbulence intensity profiles in the range of $-0.5 \le y/D \le 0.5$ are almost the same irrespective of the number of spheres. If we compare the turbulence

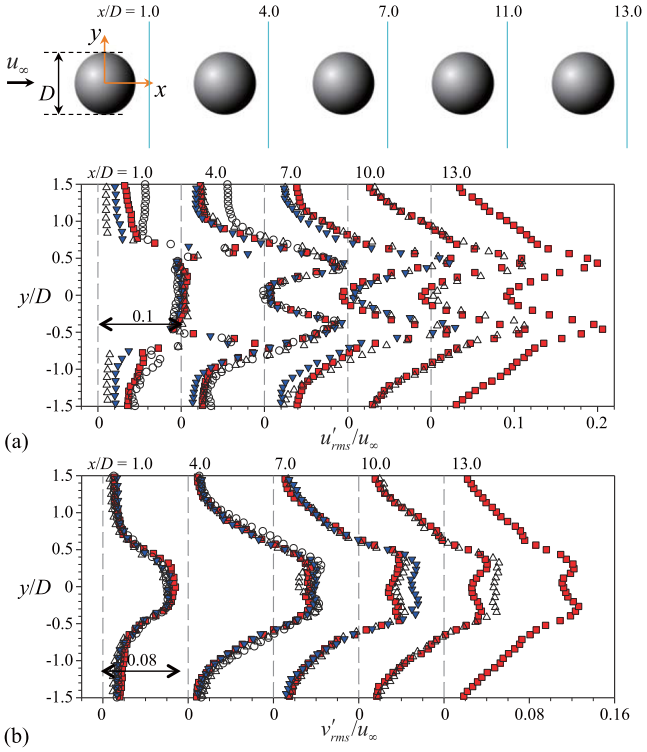

FIG. 19. Turbulence intensity profiles ($1.0D$ away from the sphere center) in a sphere array with $L/D = 2.0$: (a) streamwise turbulence intensity (u'_{rms}/u_∞) and (b) vertical turbulence intensity (v'_{rms}/u_∞). ○, two-sphere array; ▼, three-sphere array; △, four-sphere array; ■, five-sphere array.

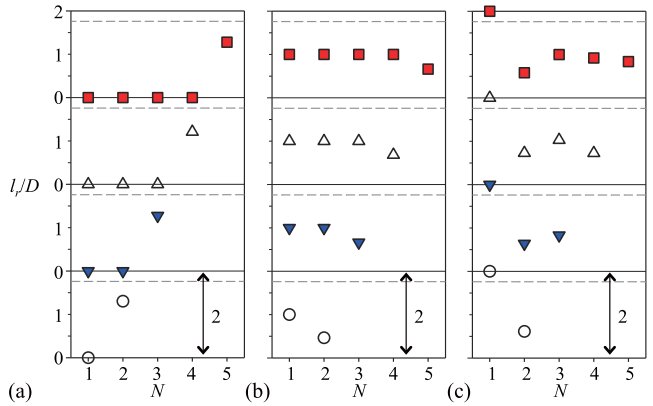

FIG. 20. Variation of the recirculation length (l_r/D) in the sphere array with (a) $L/D = 0$, (b) 1.0, and (c) 2.0. ○, two-sphere array; ▼, three-sphere array; △, four-sphere array; ■, five-sphere array. Here, N denotes the order of sphere in each condition and dashed lines denote the case of a single sphere.

at the same x/D locations with and without a trailing sphere, unlike the case of $L/D = 1.0$ (Fig. 18), it is found that the vertical turbulence intensity tends to be reduced (at $-0.5 \le y/D \le 0.5$) with a trailing sphere [Fig. 19(b)], while the streamwise component is not affected much [Fig. 19(a)]. In this condition, the separated flow from a leading sphere does not re-attach to the trailing sphere, but it just flows around the trailing sphere. Considering that most of the turbulence is contained in these shear layers, thus the turbulence intensity in the wake with a trailing sphere decreases slightly.

To quantify the effect of turbulence in the wake, which directly determines the formation of the recirculation bubble, we compare the recirculation length of each sphere wake in multiple-sphere arrays (Fig. 20). When the shear layer separated from the leading sphere re-attaches to the next sphere, i.e., the separation bubble is not completely closed, l_r is defined to be the same as the gap spacing (L). For the case of $L/D = 0$, the recirculation length is kept to be constant as zero in the gap but increases substantially in the last wake. For all sphere arrays, l_r of the last sphere is almost the same (about 75% of the single sphere wake), independent of the number of spheres [Fig. 20(a)]. When the spacing increases to $1.0D$, still the wake behind a leading sphere is not fully closed due to the trailing sphere (thus, in the gap, $l_r/D = 1.0$). However, l_r of the last wake becomes very short (less than 50% of the single sphere wake), due to the enhanced turbulence in the shear layer, which encourages the early vortex roll-up of the shear layer [Fig. 20(b)]. When the trailing sphere is outside of the separation bubble of a leading sphere, for example, of $L/D = 2.0$ [Fig. 20(c)], the l_r of the first wake is slightly longer than that of the single sphere wake. After the second wake, the recirculation bubble is reduced significantly and tends to level off to a constant value (about 50% of the single sphere wake) along the streamwise direction.

3. Effect on the Strouhal number

Finally, we discuss how the multiple spheres affect the characteristic frequency of the wake. Figure 21 shows the variation of the Strouhal number (St) in each sphere wake, measured at $x/D = 1.4$ and $y/D = 0$, for multiple-sphere arrays.

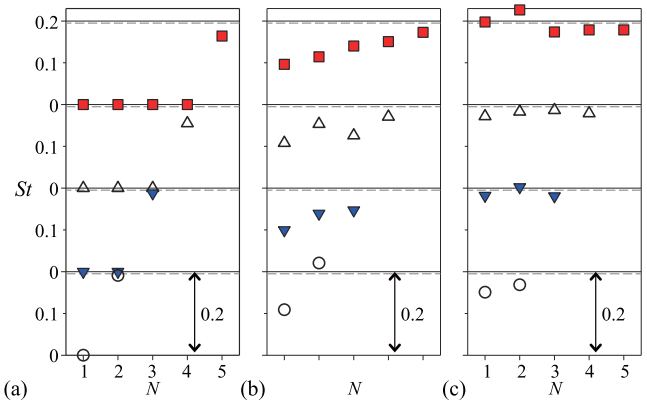

FIG. 21. Variation of the Strouhal number (St) in the sphere array with (a) L/D = 0, (b) 1.0, and (c) 2.0. ○, two-sphere array; ▼, three-sphere array; △, four-sphere array; ■, five-sphere array. Here, N denotes the order of sphere in each condition and dashed lines denote the case of the single sphere.

When $L/D = 0$, all the gap flow is stagnant ($St = 0$) and the wake of the last sphere (which is planar symmetric with a weaker turbulence level) has a clear temporal characteristic, of which St is close to that of a single sphere [Fig. 21(a)]. It is interesting to see that the last sphere wake has similar characteristic frequency to the single sphere wake even though it has a different inflow and geometry. Since the spheres are connected (L/D = 0), they may act like a single bluff body. As the distance between the spheres increases to 1.0D, unsteady flow is induced in the gap between spheres, and thus the specific frequency is captured [Fig. 21(b)]. In the first wake, St is about half of the single sphere wake (corresponding to a strong gap flow biased to the upward direction) and as the flow develops behind trailing spheres, St tends to increase gradually to reach the value of a single sphere wake. Since the shear layer evolved from the leading sphere directly attaches to the trailing sphere at this L/D, the wake of a trailing sphere would not form a well-organized structure but slowly recovers that of a single sphere. When L/D = 2.0, St of each wake almost recovers (and converges) to the single sphere wake even with increasing the number of spheres [Fig. 21(c)]. At this L/D, the first gap flow may be slightly affected by the second sphere, but the spacing is now large enough to recover the specific vortex shedding frequency in the wakes behind trailing spheres; this also agrees well with our flow visualization and velocity measurement.

V. FURTHER DISCUSSIONS

A. Estimation of the pressure distribution

So far, we have investigated how the flow around a sphere is modified by the additional spheres behind it and the spacing between them, especially focusing on the global picture of the wake structure, turbulence intensity, and frequency information. Since the fluid forces acting on each body in this kind of multi-body fluid dynamics problem are of interest as well, it would be meaningful to estimate how the loadings on each sphere would change depending on the configurations. To achieve this, we try to calculate the time-averaged pressure distribution based on the velocity field that we have measured for each condition. We start from the Navier-Stokes equation (for radial velocity u_r) in the cylindrical coordinate system,

$$\frac{\partial u_r}{\partial t} + u_r\frac{\partial u_r}{\partial r} + \frac{u_\theta}{r}\frac{\partial u_r}{\partial \theta} - \frac{u_\theta^2}{r} + u_z\frac{\partial u_z}{\partial z} = -\frac{1}{\rho}\frac{\partial p}{\partial r} + \mu\left[\frac{1}{r}\frac{\partial}{\partial r}\left(r\frac{\partial u_r}{\partial r}\right) - \frac{u_r}{r^2} + \frac{1}{r^2}\frac{\partial^2 u_r}{\partial \theta^2} + \frac{\partial^2 u_r}{\partial z^2}\right]. \tag{2}$$

Here, the origin of the coordinate system is located at the center of the first sphere in the sphere array, and the z-axis is now the streamwise direction, r is the radial direction, and θ is the circumferential direction. Thus, the velocity measurement data obtained in the Cartesian coordinate system need to be first transformed to the values in the cylindrical coordinate system. Next, the Reynolds decomposition is applied to the instantaneous velocity and pressure terms in time-averaged and fluctuating components (such as $u_r = \bar{u}_r + u_r'$ and $p = \bar{p} + p'$) and then Eq. (2) is time-averaged to obtain

$$\frac{\partial \bar{p}}{\partial r} = \rho\left[\bar{u}_r\frac{\partial \bar{u}_r}{\partial r} + \bar{u}_z\frac{\partial \bar{u}_z}{\partial z} - \frac{\partial}{\partial r}\overline{u_r'u_r'} - \frac{\partial}{\partial z}\overline{u_z'u_r'} - \frac{1}{r}\overline{u_r'u_r'} + \frac{1}{r}\overline{u_\theta'u_\theta'}\right]. \tag{3}$$

Here, the upper bar denotes the time-averaged value and $'$ is for the fluctuating one. During this formulation, the terms related to the fluid viscosity (μ) are ignored because they are much smaller than the other terms [i.e., $\boldsymbol{O}(\mu\nabla^2\bar{u}/\rho(\bar{u}\nabla)\bar{u}) \sim \boldsymbol{O}(\mu u D/\rho u^2 D^2) \sim \boldsymbol{O}(1/Re_D) \sim \boldsymbol{O}(10^{-3})$], for our condition. Although the circumferential velocity components are not available from the present measurements, we assume that $\boldsymbol{O}(\overline{u_\theta'u_\theta'}) \sim \boldsymbol{O}(\overline{u_r'u_r'})$ which has been reported by Orr *et al.* (2015). Then the equation becomes like Eq. (4), which can be integrated to get the pressure distribution with the boundary condition of $\bar{p} = 0$ at $r/D = 1.6$. This boundary where the presence of the sphere does not affect the pressure has been found from the potential flow solution. The least squares scheme (Raffel *et al.*, 2007) is used to calculate the derivative, and the trapezoidal rule (Moin, 2010) is applied for the integration,

$$\frac{\partial \bar{p}}{\partial r} = \rho\left[\bar{u}_r\frac{\partial \bar{u}_r}{\partial r} + \bar{u}_z\frac{\partial \bar{u}_z}{\partial z} - \frac{\partial}{\partial r}\overline{u_r'u_r'} - \frac{\partial}{\partial z}\overline{u_z'u_r'}\right]. \tag{4}$$

To verify the reliability of the obtained pressure field, the drag force on a single sphere (at Re_D = 1000) is estimated using the pressure field obtained by integrating Eq. (4). The force (F) acting on a single sphere is equal to the change in the momentum of the flow around the sphere (i.e., across the control volume) according to Newton's second law,

$$\vec{F} = \frac{D}{Dt}\int \rho\vec{u}\vec{u}d\vec{V}. \tag{5}$$

The source of the force acting on the control volume can be divided into the drag force (F_D) on the sphere, the pressure of the surrounding flow, and the Reynolds stress on the control surface [Eq. (6)] (Chao and van Dam, 1999),

$$-\vec{F_D} - \int \vec{p}d\vec{A} - \int \vec{\tau}d\vec{A} = \frac{D}{Dt}\int \rho\vec{u}\vec{u}d\vec{V}. \tag{6}$$

Assuming that the mean flow field is symmetric with respect to the r–z plane, finally Eq. (6) can be solved to estimate the drag

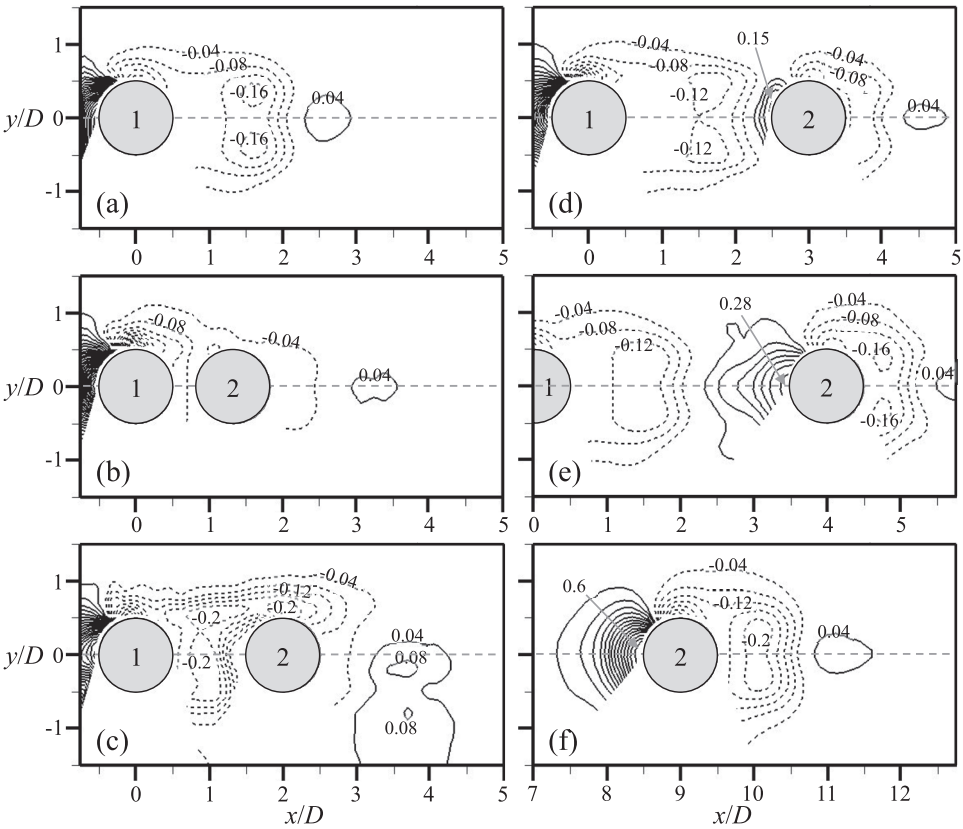

FIG. 22. Contour of the time-averaged pressure coefficient (C_p) in the flow around a two-sphere array: (a) single sphere; (b) L/D = 0.33; (c) 1.0; (d) 2.0; (e) 3.0; (f) 8.0. The contour level has an increment of 0.04 for all cases.

force (F_D) from the velocity data (Fig. 4). Figure 22(a) shows the pressure field (pressure coefficient, $C_p = 2(p - p_\infty)/\rho u_\infty^2$) for the flow around a single sphere estimated from the velocity field. It is clearly shown that there are two minima of negative C_p in the wake due to the vortex roll-up at the end of shear layers (x/D = 1.6). It is also seen that the sign of C_p changes from the negative to positive ones at the end of the recirculation zone ($x/D \simeq 2.3$). Overall, this pressure field distribution is quite similar to the previous results at Re_D = 300 in the study by Johnson and Patel (1999). In the contour, the values very near the sphere surface have been removed because the non-physical values inside the sphere are used when calculating the differential term from the mean velocity field. The cylindrical control volume is defined such as z/D = −0.7–3.0 and r/D = 1.5. Based on the pressure field in Fig. 22(a), the estimated drag coefficient of a single sphere at Re_D = 1000 is 0.47, which agrees well with 0.472, obtained by Roos and Willmarth (1971). We have also confirmed that the drag coefficient is not affected much by the choice of the control volume size. For example, when the control volume is enlarged to be z/D = −0.7–5.0 and r/D = 1.5, the drag coefficient becomes 0.46, indicating that the present estimation is more or less robust to the choice of in the size of control volume. On the other hand, we may perform a simple scaling analysis to estimate the uncertainty in the pressure estimation. Since the pressure is obtained by integrating the velocity field [Eq. (4)], the pressure scales as $p \sim \rho(U + \delta U)^2$ (U is the true value and δU is the deviation). Then the uncertainty in the pressure coefficient (C_p) is estimated as $\delta(C_p) \sim 4\delta U/U$. Here, $\delta U/U$ corresponds to the uncertainty in the velocity measurement (see Sec. II B). Thus, the uncertainty in the pressure coefficient is estimated about ±7.6%, in maximum, which agrees with the reported uncertainty range in the literature (McClure and Yarusevych, 2017).

Now, we would like to estimate the pressure (force) field in the flow around a multiple-sphere array, using the above-mentioned approach. When the number of spheres is two, the pressure distribution between the spheres varies considerably depending on the flow structure. In particular, the pressure distribution in the wake of the first sphere changes drastically; for L/D = 0.33, there is a low pressure in the stationary standing vortex in the gap between the spheres [Fig. 22(b)]. Therefore, it is expected that the second sphere would experience a lower drag force. In the second wake, a weakly low-pressure zone is formed, which is related to the planar symmetric hairpin vortex generation. When the distance between the spheres is 1.0D, an elongated low-pressure region appears due to the outgoing hairpin vortices in the upward direction from the first sphere [Fig. 22(c)]. Due to this biased pressure distribution, it is expected that the upward lift force would act on the second sphere. Also, the drag on the second sphere would become smaller because there is no strong positive pressure zone in front of the second sphere. The pressure distribution in the second wake is still asymmetric, agreeing with our flow visualization and velocity measurement. At L/D = 2.0, two low-pressure minima exist both in the first and second wakes, by the roll-up of separating shear layers [Fig. 22(d)]. At this condition, the drag force on the first sphere is predicted to be similar to that of a single sphere although the shear layer roll-up is interfered by the second sphere. However, the drag on the second sphere would be still smaller than that of a single sphere. When the distance between the spheres increases

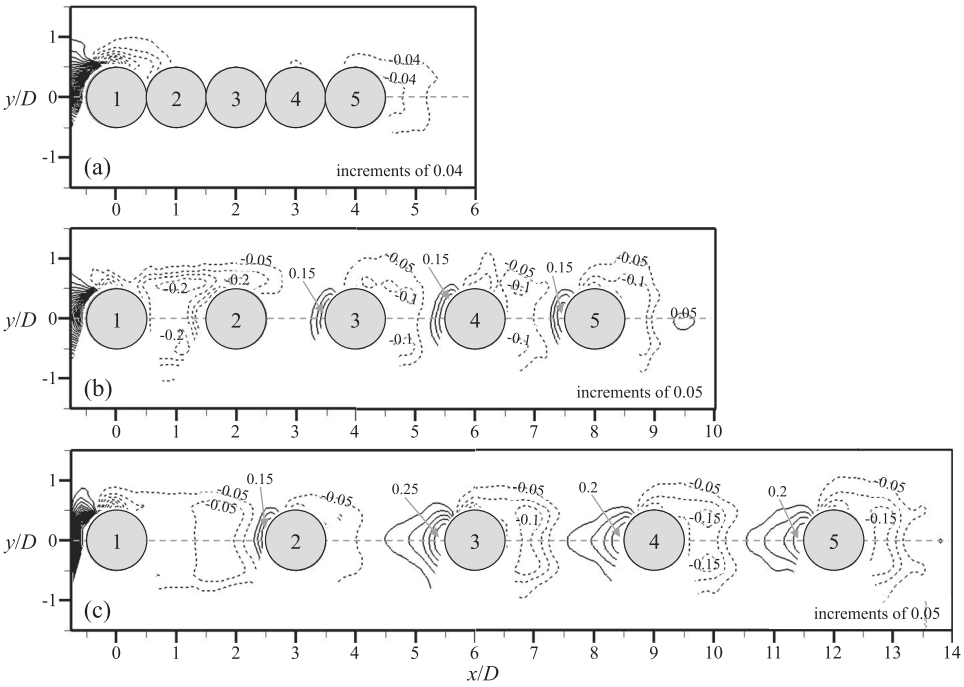

FIG. 23. Contour of the time-averaged pressure coefficient (C_p) in the flow around a five-sphere array: (a) $L/D = 0$; (b) 1.0; (c) 2.0.

further ($L/D \geq 3.0$), the trailing sphere is outside of the recirculation bubble of a leading sphere, and thus a strong positive (stagnation) pressure is induced in front of the second sphere [Figs. 22(e) and 22(f)]. This stagnant pressure increases with increasing L/D, and the wake of the second sphere becomes much more similar to the wake of a single sphere.

Figure 23 shows the pressure coefficient (C_p) distribution around a five-sphere array depending on L/D. When the spheres are in contact with each other (although the wakes between the spheres are difficult to observe due to the limited resolution of pressure estimation), there is a weak low-pressure region in the last wake, which is contributed by the planar symmetric hairpin vortex [Fig. 23(a)]. As the spacing increases to 1.0D, the high pressure zone tends to recover from the third sphere [Fig. 23(b)], and the overall shape of the pressure distribution also becomes symmetric. It can be inferred that from the third sphere, it will receive a stronger force (i.e., drag) than the second one. This tendency has also been reported in the simulation for the flow around a three-sphere array ($L/D < 1.0$) (Liang *et al.*, 1996 and Maheshwari *et al.*, 2006). However, all of them will experience a smaller drag than the first sphere. As L/D increases to 2.0, the pressure distribution becomes almost axisymmetric [Fig. 23(c)]. From the third sphere, the high-pressure region in front of the sphere is restored and the same pressure distribution is retained to the fifth sphere. The drag forces on the third-to-fifth spheres are expected to reach closer to that of a single sphere. It is noted that the second sphere would receive the smallest drag in this five-sphere array due to the negative pressure on its front.

B. Classification of the flow regime

Collecting all the trends in the flows around a multiple-sphere array, considered in the present study, in Fig. 24, we suggest a wake flow classification depending on the number of spheres, spacing between them, and the order of wake (wake sequence) in the array. As we have already mentioned, we use three criteria: turbulence level, flow symmetry, and Strouhal number. Here, regime I is a planar symmetric wake with a weaker turbulence level and comparable St (compared to the single sphere wake), regime II is a planar symmetric wake with moderate turbulence [St is about twice as large (small) as a single sphere wake in the shear layer (gap), respectively], and regime III is an axisymmetric wake with a turbulence level and St comparable to the single sphere wake. In addition, regime 0 (axisymmetric and quasi-steady wake) is defined. For the reference, the single sphere wake at $Re_D = 1000$ belongs to regime III. When the spacing is $L/D = 0$ and 0.33, the wakes between spheres are steady and axisymmetric. However, the last wake sheds planar symmetric vortices with a specific St

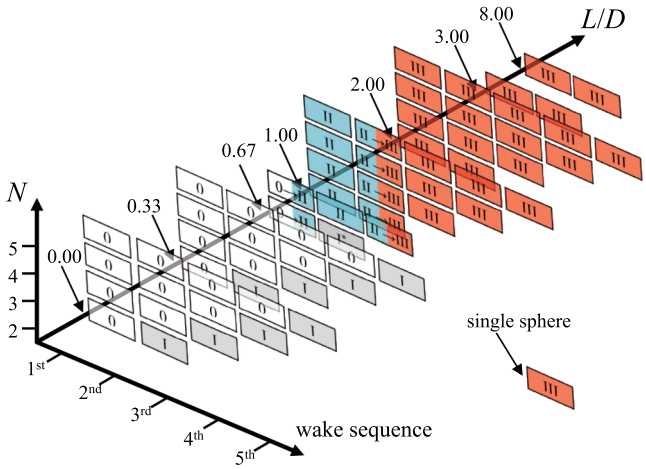

FIG. 24. Flow regime map of the wake in an in-lined sphere array according to the number of spheres (N), the spacing between adjacent spheres (L/D), and the wake sequence in each condition: regime 0, axisymmetric and quasi-steady wake; regime I, weaker turbulence and planar symmetric wake; regime II, moderate turbulence and planar symmetric wake; regime III, turbulence level similar to the single sphere and axisymmetric.

around 0.2 and has a lower turbulence level compared to a single sphere wake. For a narrow range of L/D around 0.67, all wakes experience the flow transition (from regimes 0 to II). It sheds planar vortices having a weaker turbulence but in alternative directions according to the shedding direction in a leading wake. The wake of the second sphere (if there is no third sphere) produces hairpin vortices and has a low turbulence intensity (similar to regime I). However, the direction of the hairpin vortex head changes alternately (not constant) in both directions which is different from regime I (thus marked as regime I*). In the case of a three-sphere array, a rapid change in the flow regime occurs along the streamwise direction. The second wake has a strong asymmetric gap flow and vortex generation (as in regime II), and the third wake experiences a transition from the asymmetric to axisymmetric flow structure. When the spacing is 1.0D, the first wake sheds vortices in the upward direction, thus forming a statistically planar symmetric wake. Above the spacing of 2.0D, all wakes are classified as regime III, which is characterized by an axisymmetric wake with the same level of turbulence as the wake of a single sphere.

From this regime classification, it is understood that if the distance between spheres is long enough ($L/D \gtrsim 2.0$) or very short ($L/D \lesssim 0.33$), the sphere wakes are mainly axisymmetric. Between these ranges ($0.67 \lesssim L/D \lesssim 1.0$), the flow structure becomes asymmetric. We also observed strong convergence to an axisymmetric wake structure with increasing L/D and the order of wake sequence. Despite a strong asymmetry in the first wake, for example, for $L/D = 1.0$, the axisymmetry (regime III) appears from the third wake. The convergence in the symmetry of the spherical wake in such a sphere array may be useful in simplifying the wake model. Previously, relevant two-phase flow models have been developed under the assumption that the wake of a particle (assumed to be spherical) is axisymmetric in gas-liquid (Riboux *et al.*, 2013 and Kim *et al.*, 2015) and solid-gas flows (Zaidi, 2018). If the dispersed phase is dense, it is not clear whether the axisymmetric assumption is valid. However, the present results show that the sphere wake is axisymmetric even if the spacing between the dispersed phases is as small as its size. In terms of the fluid force, there would be a negligible drag and lift forces in regime 0, which will increase in regime I with an asymmetric wake. In regime II, the instantaneous lift force will be determined by the direction of hairpin vortex shedding, and the drag force will be smaller than that of a single sphere. A sphere in regime III will receive a similar or smaller drag (except the first sphere in the array) than a single sphere.

VI. CONCLUDING REMARKS

In the present study, the flow around an in-line sphere array at $Re_D = 1000$ has been experimentally investigated while varying the number of spheres (1-5 spheres) and the spacing between them (L/D = 0–3.0). We used dye visualization and particle image velocimetry techniques. First, we have observed how the wakes of the first and second spheres in a two-sphere array change depending on the distance between them, and it was classified into four flow types based on the flow symmetry, turbulence intensity level, and the characteristic frequency. When two spheres are very close ($L/D \leq 0.33$), the first wake has a standing vortex (steady and axisymmetric) and the second wake is planar symmetric (the frequency of this wake is equal to the wake of a single sphere). As the spacing between the spheres increases ($L/D = 1.0$), the wake of the first sphere loses its axisymmetric property and produces a planar symmetric hairpin vortex with strong turbulence intensity in one direction. The second wake receives a large perturbation due to the hairpin vortex generated upstream. However, based on quantitative turbulence measurements, this wake is statistically close to be axisymmetric. For a larger spacing of $L/D \geq 2.0$, the wake of leading spheres becomes statistically axisymmetric and sheds hairpin vortices. Based on this classification, next we observed how the wake of the added sphere changes as the number of spheres increases while maintaining the spacing between them. As a result, all the wakes of each sphere constituting the sphere array could be classified according to the same regime classification. For the spacing of 0D and 0.33D, regardless of the number of spheres, a standing vortex (regime 0) occurs in the gap between the spheres, and a planar symmetric hairpin vortex with low turbulence intensity occurs periodically in the wake of the last sphere with a comparable frequency of the single sphere wake (regime I). When the spacing between the spheres is 1.0D, a wavy hairpin vortex in one direction is induced in the first wake, which is planar symmetric (regime II). From the third wake, however, it was confirmed that all of them are axisymmetric flow structures. Similarly, when the distance between the spheres is 2.0–3.0D, the wakes of all spheres are axisymmetric (regime III).

To understand the result of flow modification further, the pressure field in the flow around a sphere array was estimated from the measured velocity field. This allowed us to quantitatively estimate the magnitude and direction of the force depending on the type of wake in each sphere array. The force on the sphere with the wake of regime 0 is difficult to predict due to the limitation of resolution. However, the sphere with the wake of regime I is expected to experience a weak lift force due to the asymmetric (planar symmetric) wake. The sphere in regime II, on the other hand, would receive a stronger lift, and the one in regime III does not receive a lift but is expected to experience a smaller drag force than a single sphere.

The flow around a sphere is a very well-known problem in fluid dynamics, but the present situation where multiple of them exist nearby has not been investigated in detail. Considering the rising importance of multi-body fluid dynamics, we believe that the findings of the present study will be further extended to understand the mechanism of interaction between dispersed phases in a multiphase flow (Fortes *et al.*, 1987). In particular, it may be used to explain the tumbling phenomenon in the rising bubbles. To assist this, more follow-up investigations on different Reynolds numbers and particle (sphere) arrangements would be required, as future work.

ACKNOWLEDGMENTS

This research was supported by a grant (No. KCG-01-2017-02) through the Disaster and Safety Management Institute funded by the Korea Coast Guard of Korean

government and research grants (Nos. 2016R1C1B2012775, 2017M2A8A4018482, 2017R1A4A1015523, and 2016M2B-2A9A02945068) through the National Research Foundation of Korea (NRF), funded by the Korea government via SNU-IAMD.

Achenbach, E., "The effect of surface roughness and tunnel blockage on the flow past spheres," J. Fluid Mech. **65**, 113–125 (1974).
Bagchi, P. and Balachandar, S., "Response of the wake of an isolated particle to an isotropic turbulent flow," J. Fluid Mech. **518**, 95–123 (2004).
Blackman, K. and Perret, L., "Non-linear interactions in a boundary layer developing over an array of cubes using stochastic estimation," Phys. Fluids **28**, 095108 (2016).
Cebeci, T. and Kafyeke, F., "Aircraft icing," Annu. Rev. Fluid Mech. **35**, 11–21 (2003).
Chao, D. D. and van Dam, C. P., "Airfoil drag prediction and decomposition," AIAA J. **36**, 675–681 (1999).
Chen, R. C. and Lu, Y. N., "The flow characteristics of an interactive particle at low Reynolds numbers," Int. J. Multiphase Flow **25**, 1645–1655 (1999).
Choi, H., Jeon, W.-P., and Kim, J., "Control of flow over a bluff body," Annu. Rev. Fluid Mech. **40**, 113–139 (2008).
Folkersma, R., Stein, H. N., and van de Vosse, F. N., "Hydrodynamic interactions between two identical spheres held fixed side by side against a uniform stream directed perpendicular to the line connecting the spheres' centres," Int. J. Multiphase Flow **26**, 877–887 (2000).
Fortes, A. F., Joseph, D. D., and Lundgren, T. S., "Nonlinear mechanics of fluidization of beds of spherical particles," J. Fluid Mech. **177**, 467–483 (1987).
Gerrard, J. H., "The mechanics of the formation region of vortices behind bluff bodies," J. Fluid Mech. **25**, 401–413 (1966).
Hamilton, N., Tutkun, M., and Cal, R. B., "Low-order representations of the canonical wind turbine array boundary layer via double proper orthogonal decomposition," Phys. Fluids **28**, 025103 (2016).
Happel, J. and Pfeffer, R., "The motion of two spheres following each other in a viscous fluid," AIChE J. **6**, 129–133 (1960).
Hoomans, B. P. B., Kuipers, J. A. M., Briels, W. J., and van Swaaij, W. P. M., "Discrete particle simulation of bubble and slug formation in a two-dimensional gas-fluidised bed: A hard-sphere approach," Chem. Eng. Sci. **51**, 99–118 (1996).
Hooshanginejad, A. and Lee, S., "Droplet depinning in a wake," Phys. Rev. Fluids **2**, 031601(R) (2017).
Jadoon, A., Prahl, L., and Revstedt, J., "Dynamic interaction of fixed dual spheres for several configurations and inflow conditions," Eur. J. Mech.: B/Fluids **29**, 43–52 (2010).
Jeong, H. and Park, H., "Near-wall rising behaviour of a deformable bubble at high Reynolds number," J. Fluid Mech. **771**, 564–594 (2015).
Johnson, T. and Patel, V. C., "Flow past a sphere up to a Reynolds number of 300," J. Fluid Mech. **378**, 19–70 (1999).
Kim, H. J. and Durbin, P. A., "Observations of the frequencies in a sphere wake and of drag increase by acoustic excitation," Phys. Fluids **31**, 3260–3265 (1988).
Kim, I., Elghobashi, S., and Sirignano, W. A., "Three-dimensional flow over two spheres placed side by side," J. Fluid Mech. **246**, 465–488 (1993).
Kim, M., Lee, J. H., and Park, H., "Study of bubble-induced turbulence in upward laminar bubbly pipe flows measured with a two-phase particle image velocimetry," Exp. Fluids **57**, 55 (2016).
Kim, N., Kim, H., and Park, H., "An experimental study on the effects of rough hydrophobic surfaces on the flow around a circular cylinder," Phys. Fluids **27**, 085113 (2015).
Kimball, E., Whitaker, T., Kevrekidis, Y. G., and Benziger, J. B., "Drops, slugs, and flooding in polymer electrolyte membrane fuel cells," AIChE J. **54**, 1313–1332 (2008).
Kumar, S. S. P., Patnaik, B. S. V., and Ramamurthi, K., "Prediction of air blast mitigation in an array of rigid obstacles using smoothed particle hydrodynamics," Phys. Fluids **30**, 046105 (2018).
Lawson, N. J., Rudman, M., Guerra, A., and Liow, J. L., "Experimental and numerical comparisons of the break-up of a large bubble," Exp. Fluids **26**, 524–534 (1999).
Lee, J., Kim, H., and Park, H., "Effects of superhydrophobic surfaces on the flow around an NACA0012 hydrofoil at low Reynolds numbers," Exp. Fluids **59**, 111 (2018).
Lee, J. and Park, H., "Wake structures behind an oscillating bubble rising close to a vertical wall," Int. J. Multiphase Flow **91**, 225–242 (2017).
Lee, K. C., "Aerodynamic interaction between two spheres at Reynolds numbers around 10^4," Aeronaut. Q. **30**, 371–385 (1979).
Liang, S. C., Hong, T., and Fan, L. S., "Effects of particle arrangements on the drag force of a particle in the intermediate flow regime," Int. J. Multiphase Flow **22**, 285–306 (1996).
Madani, S. and Amirfazli, A., "Oil drop shedding from solid substrates by a shearing liquid," Colloids Surf., A **441**, 796–806 (2014).
Magnaudet, J. and Mougin, G., "Wake instability of a fixed spheroidal bubble," J. Fluid Mech. **572**, 311–337 (2007).
Maheshwari, A., Chhabra, R. P., and Biswas, G., "Effect of blockage on drag and heat transfer from a single sphere and an in-line array of three spheres," Powder Technol. **168**, 74–83 (2006).
McClure, J. and Yarusevych, S., "Optimization of planar PIV-based pressure estimates in laminar and turbulent wakes," Exp. Fluids **58**, 62 (2017).
Mittal, R., Wilson, J. J., and Najjar, F. M., "Symmetry properties of the transitional sphere wake," AIAA J. **40**, 579–582 (2002).
Moin, P., *Fundamentals of Engineering Numerical Analysis* (Cambridge University Press, 2010).
Monkewitz, P. A. and Nguyen, L. N., "Absolute instability in the near-wake of two-dimensional bluff bodies," J. Fluids Struct. **1**, 165–184 (1987).
Orr, T. S., Domaradzk, J. A., Spedding, G. R., and Constantinescu, G. S., "Numerical simulations of the near wake of a sphere moving in a steady, horizontal motion through a linearly stratified fluid at Re = 1000," Phys. Fluids **27**, 035113 (2015).
Park, H., Lee, D., Jeon, W.-P., Hahn, S., Kim, J., Kim, J., Choi, J., and Choi, H., "Drag reduction in flow over a two-dimensional bluff body with a blunt trailing edge using a new passive device," J. Fluid Mech. **563**, 389–414 (2006).
Pier, B., "Local and global instabilities in the wake of a sphere," J. Fluid Mech. **603**, 39–61 (2008).
Prahl, L., Jadoon, A., and Revstedt, J., "Interaction between two spheres placed in tandem arrangement in steady and pulsating flow," Int. J. Multiphase Flow **35**, 963–969 (2009).
Raffel, M., Willert, C. E., Wereley, S., and Kompenhans, J., *Particle Image Velocimetry: A Practical Guide* (Cambridge University Press, 2007).
Riboux, G., Legendre, D., and Risso, F., "A model of bubble-induced turbulence based on large-scale wake interactions," J. Fluid Mech. **719**, 362–387 (2013).
Roos, F. W. and Willmarth, W. W., "Some experimental results on sphere and disk drag," AIAA J. **9**, 285–291 (1971).
Roshko, A., "On the wake and drag of bluff bodies," J. Aeronaut. Sci. **22**, 124 (1955).
Sakamoto, H. and Haniu, H., "A study on vortex shedding from spheres in a uniform flow," J. Fluids Eng. **112**, 386–392 (1990).
Scarano, F., "Iterative image deformation methods in PIV," Meas. Sci. Technol. **13**, R1 (2001).
Schouveiler, L., Brydon, A., Leweke, T., and Thompson, M. C., "Interactions of the wakes of two spheres placed side by side," Eur. J. Mech.: B/Fluids **23**, 137–145 (2004).
Shi, X. and Christopher, G. F., "Growth of viscoelastic instabilities around linear cylinder arrays," Phys. Fluids **28**, 124102 (2016).
Soltani, M. and Ahmadi, G., "On particle adhesion and removal mechanisms in turbulent flows," J. Adhes. Sci. Technol. **8**, 763–785 (1994).
Taneda, S., "Experimental investigation of the wakes behind cylinders and plates at low Reynolds numbers," J. Phys. Soc. Jpn. **11**, 302–307 (1956).
Testik, F. Y. and Ungarish, M., "On the self-similar propagation of gravity currents through an array of emergent vegetation-like obstacles," Phys. Fluids **28**, 056605 (2016).
Tomboulides, A. G. and Orszag, S. A., "Numerical investigation of transitional and weak turbulent flow past a sphere," J. Fluid Mech. **416**, 45–73 (2000).
Tsuji, T., Morikawa, Y., and Terashima, K., "Fluid-dynamic interaction between two spheres," Int. J. Multiphase Flow **8**, 71–82 (1982).
Tsuji, T., Narutomi, R., Yokomine, T., Ebara, S., and Shimizu, A., "Unsteady three-dimensional simulation of interactions between flow and two particles," Int. J. Multiphase Flow **29**, 1431–1450 (2003).
Uhlmann, M. and Doychev, T., "Sedimentation of a dilute suspension of rigid spheres at intermediate Galileo numbers: The effect of clustering upon the particle motion," J. Fluid Mech. **752**, 310–348 (2014).
Westerweel, J. and Scarano, F., "Universal outlier detection for PIV data," Exp. Fluids **39**, 1096–1100 (2005).
Williamson, C. H. K., "Vortex dynamics in the cylinder wake," Annu. Rev. Fluid Mech. **28**, 477–539 (1996).
Wu, J. S. and Faeth, G. M., "Sphere wakes in still surroundings at intermediate Reynolds numbers," AIAA J. **31**, 1448–1455 (1993).

Yoon, D. H. and Yang, K. S., "Flow-induced forces on two nearby spheres," Phys. Fluids **19**, 098103 (2007).
Yoon, D. H. and Yang, K. S., "Characterization of flow pattern past two spheres in proximity," Phys. Fluids **21**, 073603 (2009).
Yun, G., Kim, D., and Choi, H., "Vortical structures behind a sphere at subcritical Reynolds numbers," Phys. Fluids **18**, 015102 (2006).
Zaidi, A. A., "Study of particle inertia effects on drag force of finite sized particles in settling process," Chem. Eng. Res. Des. **132**, 714–728 (2018).
Zhu, C., Liang, S. C., and Fan, L. S., "Particle wake effects on the drag force of an interactive particle," Int. J. Multiphase Flow **20**, 117–129 (1994).
Zhu, H. P., Zhou, Z. Y., Yang, R. Y., and Yu, A. B., "Discrete particle simulation of particulate systems: Theoretical developments," Chem. Eng. Sci. **62**, 3378–3396 (2007).
Zou, J. F., Ren, A. L., and Deng, J., "Study on flow past two spheres in tandem arrangement using a local mesh refinement virtual boundary method," Int. J. Numer. Methods Fluids **49**, 465–488 (2005).